ELSEVIER

Contents lists available at ScienceDirect

Surface & Coatings Technology

journal homepage: www.elsevier.com/locate/surfcoat



Full Length Article



Effect of TiC content on the microstructure and wear performance of in situ synthesized Ni-based composite coatings by laser direct energy deposition

Liaoyuan Chen ^a, Yu Zhao ^b, Fanwei Meng ^a, Tianbiao Yu ^{a,*}, Zhelun Ma ^a, Sheng Qu ^a, Zhengyu Sun ^a

- ^a School of Mechanical Engineering and Automation, Northeastern University, Shenyang, China
- ^b School of Mechanical Engineering and Aerospace Engineering, Jilin University, Changchun, Jilin, China

ARTICLE INFO

Keywords: LDED In situ synthesis Size and content of TiC Phase evolution Microhardness Wear resistance

ABSTRACT

To reveal the effect of content and size of in situ synthesized TiC on phase compositions, microstructure, defects, and mechanical properties of matrix composites in detail, a series of Ni-based composite coatings were fabricated by direct energy deposition. The titanium (Ti) + Ni-coated graphite (C) contents in composite powder are 5, 10, 20, 30, 40, and 50 wt%, respectively. With the increase of Ti and C elements, the phases firstly change from γ -Ni, [Fe-Ni] solid solution, CrB, Cr γ C3 to [Fe-Ni] solid solution, CrB, Cr γ C3, TiNi $_2$ TiC, TiB $_2$, and finally to TiNi, Cr $_3$ C2, Fe $_2$ Ti, TiC, TiB $_2$ under the competitive interaction between solute concentration and Gibbs free energy. The volume fraction and relative diameter of the TiC reinforcements are increased gradually to 28.06 % and 2.866 μ m, respectively. The dispersed TiC particles are found at the grain boundary and refine the grains. The microhardness is increased from 608.41 \pm 6.25 HV $_{0.3}$ to 1075.11 \pm 27.94 HV $_{0.3}$ due to the combined effect of fine-grain strengthening, solid solution strengthening, and the second phase strengthening. The volume loss was significantly reduced when the relative diameter of TiC is larger than 2.2 μ m. Moreover, the wear mechanism was transformed from adhesive wear to abrasive wear and ultimately to fatigue wear. In addition, the transverse and longitudinal cracks were also observed, limiting the application of the fabricated coatings.

1. Introduction

Nickel (Ni) or Ni-based alloys have been applied on turbo-engines, a nozzle of aviation engines, and various components in the corrosion resistance field [1], owning to excellent high-temperature stability, corrosion resistance, and plasticity [2,3]. However, the defects, such as cavitation, abrasive or adhesive wear, etc. [4], would appear on the surface of these Ni-based parts with low hardness and poor wear resistance [5]. Nickel matrix composites (NMC) have received a lot of attention from engineers and researchers [6] because they have been proven to achieve comprehensive mechanical properties by combining excellent wear resistance [7] and good toughness [8]. Laser direct energy deposition (LDED) is a well-known metal additive manufacturing (AM) advancement due to its inherent merits such as small heat-affected zone, good metallurgical bonding properties, and flexible design of deposition material and strategy [9,10]. Therefore, LDED has been widely employed for the manufacture of complex structures or surface modification and repair of mechanical parts [11,12].

The ceramic materials have been proved as ideal reinforcements for LDED NMC coatings due to their high hardness, good wear resistance, and thermal stability [13,14]. Therefore, the microhardness, wear resistance, and corrosion resistance have been improved by introducing TiC, TiB₂, WC, TiN, B₄C, SiC, and Al₂O₃ ceramic particles, benefitting from grain refinement, dispersion strengthening, and solid solution strengthening [15,16]. The TiC-reinforced NMC by LDED has received a great deal of attention due to the superior wetting behavior between the TiC and Ni-based alloy [17,18].

Saroj et al. [19] reported the effects of TiC content, preplaced layer thickness, and processing current on the molten pool lifetime, microstructure, and mechanical performance of the TiC-Inconel825 composite coating. More pores, poor wetting, and bonding between the TiC particles and the matrix are found in clad tracks because of shorter molten pool lifetimes. Yu et al. [20] optimized the process parameters of coaxial LDED customized precursors including 10 wt% TiC and commercial Ni45 powder by using empirical statistical models and the Taguchi method. Although microhardness of single-layer multi-tracks TiC

^{*} Corresponding author at: School of Mechanical Engineering and Automation, Northeastern University, Shenyang, 110819, China. *E-mail address:* tianbiaoyudyx@gmail.com (T. Yu).

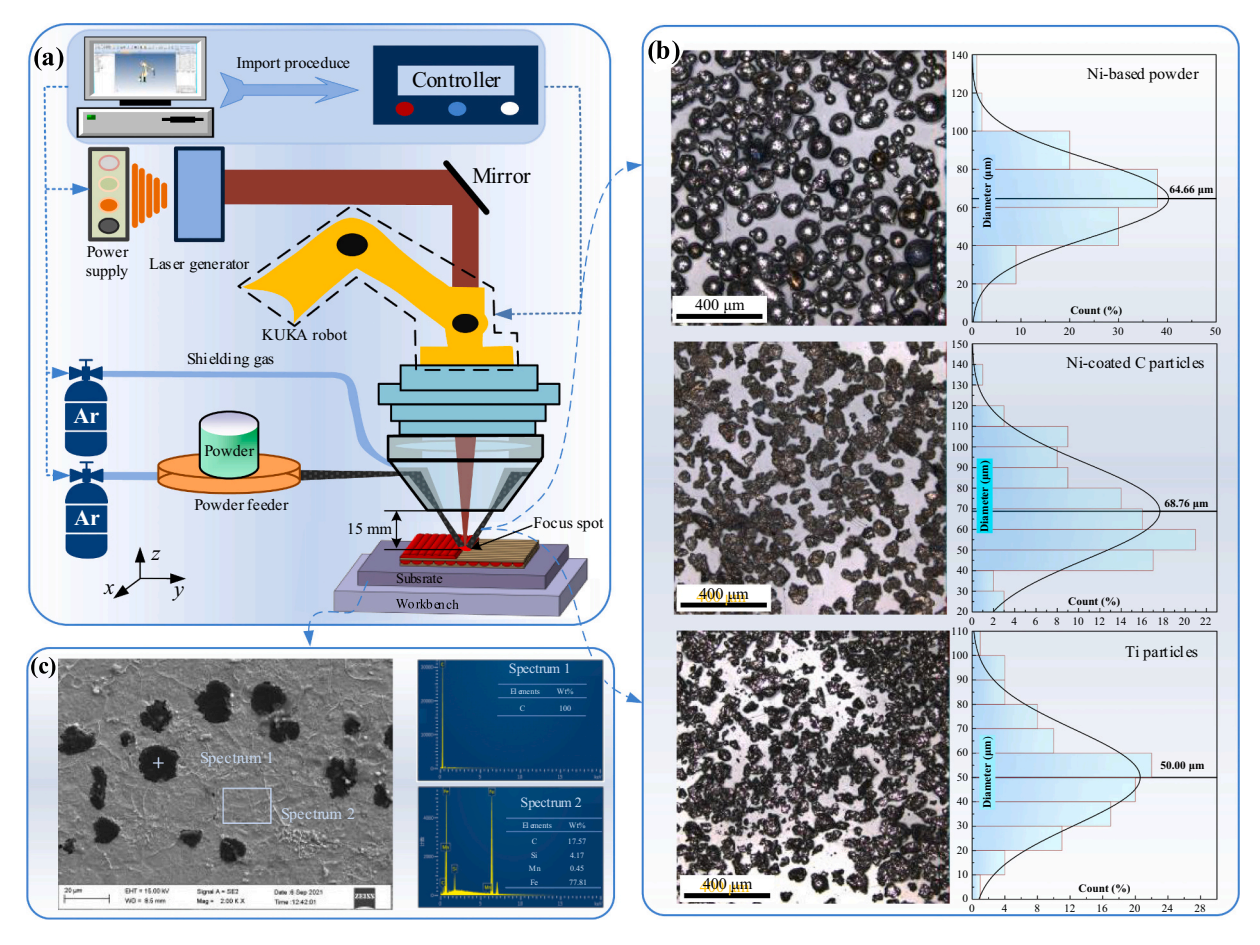


Fig. 1. (a) Schematic diagram of the LDED process, (b) particle morphologies and size statistics, (c) SEM image and EDS results of the substrate.

reinforced Ni-based composite coatings is 2.5 times that of origin coating. Besides, microhardness uniformity along the build and grind directions was also observed due to the incomplete melting of coarse TiC particles. Gopinath et al. [18,21] established a relation between the process parameter and mechanical properties for preset Inconel 718/TiC composite powders via laser cladding. The shorter melt pool lifetime results in high porosity, poor wetting between the TiC and the matrix. On the contrary, the TiC particles can be completely decomposed when the molten pool lifetime exceeds 0.45 s. To repair damaged spline shaft using the additive/subtractive hybrid manufacturing technology, Chen et al. [15] firstly compared the effects of coarse TiC content on the microstructure and mechanical properties of the NMC coating. Wear resistance in the repaired zone with the addition of 30 wt% TiC+6 wt% TiN is only 0.304 times that of the substrate. However, some pits were also found on the worn surface due to spalling of coarse TiC.

Previous studies have found that the hardness and wear resistance of NMC coatings can be improved owing to the addition of ceramic particles. Besides, the microstructure and mechanical properties of these NMC coatings highly depend on the size and volume fraction of ceramic particles. Coarse ceramic particles significantly improve the wear resistance of NMC, while fine ceramic particles are more advantageous in terms of uniform mechanical properties [22]. On the one hand, directly added coarse ceramics can be difficult to melt completely due to their high melting point and short life of the melt pool. Therefore, ceramics tend to aggregate under the action of strong Marangoni convection due to the big mismatch in density. This phenomenon would be more serious when the volume fraction of ceramics is low. Therefore, the step in the mechanical properties between the unmelted coarse ceramics and matrix are present, weakening the fatigue life of the materials [23]. On the other hand, fine ceramic particles embedded in the matrix are

easily removed during the wear process. As a result, the wear resistance of the composite coating is significantly reduced. Therefore, the in situ synthesized ceramics reinforced NMC coatings fabricated by LDED have received extensive attention because of their homogeneous distribution and good wetting to the matrix.

Cui et al. [24] confirmed that dispersed in situ TiC particles can be introduced by laser deposition preset Ni-Ti-C composite powder. When the content of Ti + C in composite powders is increased from 8 wt% to 20 wt%, the hardness of the composite coating is increased from 40.0 HRC to 59.5 HRC. Hamedi et al. [25] fabricated TiC-reinforced composite coatings by laser melting graphite layer with the thickness of 300 μm on the surface of a commercial titanium plate. As the laser energy increase, the micro-hardness of the NMC coating increases from 425 HV to 1700 HV, which is 10 times that of the substrate. Chen et al. [26] fabricated in situ Ti(C, N) reinforced NMC coatings by laser deposition preset Ni60, C, and TiN mixed powders on Ti6Al4V alloys. Besides, the generation mechanism of Ti(C, N) and the strengthening mechanism are also revealed. To improve the wear resistance of Ni204 alloy, Zhao et al. [4,27] has developed a series of ceramic (TiC, TiN, and B_4C) particles reinforced NMC coatings. The ring phase (Ti, Mo, Nb) (C, N), Ti(C, N), and MCx were in situ synthesized. The microhardness is increased from about 200 HV to about 1100 HV. Besides, the friction coefficient of NMC coating is 0.225 times that of the original Ni204 coating. With the aid of experiments [28], thermodynamic calculations [29], and simulation models [30], the mechanism, fabricating process, and practical application of in situ ceramic particles reinforced NMC coatings have been revealed in detail. Nevertheless, the researchers also found that the microhardness, toughness, and wear resistance of NMC coatings are highly dependent on the size and content of the ceramic particles. However, a systematic study on the effect of size and TiC content on

Table 1Experimental design for NMC coating and LDED process parameters.

Coating	Composition design			LDED process p	LDED process parameters						
	Ni-based powder	Ti particle	Ni-coated C particle	Laser power (W)	Scanning speed (mm/s)	Powder feed rate (r/min)	Track space (mm)	Z-axis increment (mm)			
S0	0	0	0	425	4.5	0.85	0.6	0.5			
S5	95	3.75	1.25								
S10	90	7.49	2.51								
S20	80	14.98	5.02								
S30	70	22.47	7.53								
S40	60	29.96	10.04								
S50	50	37.45	12.55								

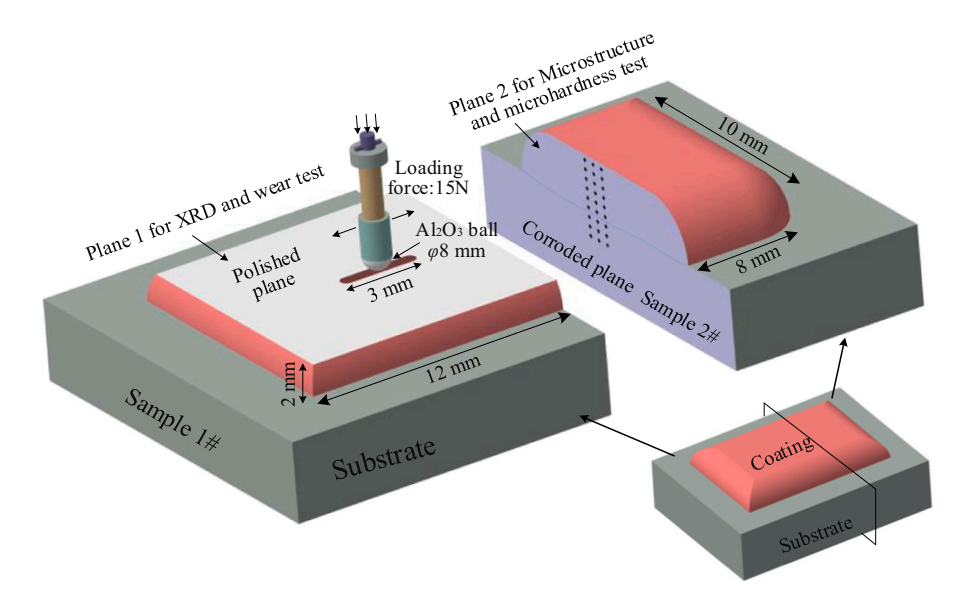


Fig. 2. Schematic diagram of test samples preparation process.

microstructure and mechanical properties of NMC coatings is rarely carried out.

Herein, based on the strong affinity of titanium (Ti) with graphite (C) and good wetting between the TiC and Ni alloy, the Ti + Ni-coated C particles with gradient contents were mixed in Ni-based alloy powders, and then a series of in situ TiC reinforced NMC coatings were fabricated by LDED in this study. The synergistic effect of content and size of TiC reinforcements on phases characterization, microstructures, defects, microhardness, and wear resistance of NMC coatings was elucidated in detail. Moreover, the solidification process and morphologies of the solidified reinforcements in NMC coatings were demonstrated by the competing thermodynamic and solute concentrations. Besides, the strengthening mechanism of microhardness and wear resistance of as-LDMD coatings are also discussed in detail.

2. Experimental

2.1. Material and method

The setup used in this study is a coaxial LDED system [31], as shown in Fig. 1a. The maximum power and wavelength of the CW fiber laser source are 500 W and 1020 nm, respectively. The focal length of the laser with Gaussian distribution is 55 mm. As shown in Fig. 1a, the distance from the laser focus spot to the bottom of the cladding head is 15 mm, whereas the diameter of the laser beam is 1.0 mm. The strategy of four-layers coating with the scanning direction between the layers at 90° follows a rectangle with a length of 20 mm and a width of 10 mm. The previous study [32] has reported that this scanning strategy could homogenize the heat flow between the different layers. The chemical

composition of the Ni-based self-fluxing powder is 0.45 C, 12.00 Cr, 4.00 Si, 0.10 Mn, 2.40 B, 1.00 wt% Fe, and balance Ni. Since low-density graphite (C) particles were difficult to be transported into the molten pool, Ni-coated C particles (mass ratio of Ni to C = 1:3) were selected in this study. The optical images and size statistics of Ni-based powder, Nicoated C, and Ti particles (purity >99.5 %) are shown in Fig. 1b. The precursors were divided into seven groups according to increasing Ti + C content. Besides, the atomic ratio of Ti to C is 1:1 in each designed sample. Table 1 lists the detailed component design and LDED process parameters. Besides, the shielding gas and the powder feed gas are argon of 99.99 % purity at a flow rate of 20 L/min and 10 L/min, respectively. The precursor was mixed in a planetary ball mill for 2 h, respectively. The substrate is nodular cast iron with a size of $100 \times 100 \times 10 \text{ mm}^3$. The field emission scanning electron microscopy (SEM; Zeiss, Germany) image and energy dispersive spectroscopy (EDS) results of the substrate are shown in Fig. 1c. Before the experiment, all precursors were dried at 100 °C for 2 h to remove water vapor. Besides, the substrate surface was ground with 800 grit sandpaper and then cleaned with alcohol to remove dirt.

2.2. Characterization

Fig. 2 illustrates the schematic diagram of the test samples preparation process. After the LDED process, sample 1# for the wear test and sample 2# for microstructure were cut from the substrate by an electrical discharge machine (EDM). Plane 1 of sample 1# was ground by SiC papers up to 2000 grit, and then polished using the diamond polishing paste with the size of $2~\mu m$. Plane 2 of sample 2# was chemically etched with an aqua regia (HCl: $HNO_3 = 3:1$ in vol.) for 25-40 s. All

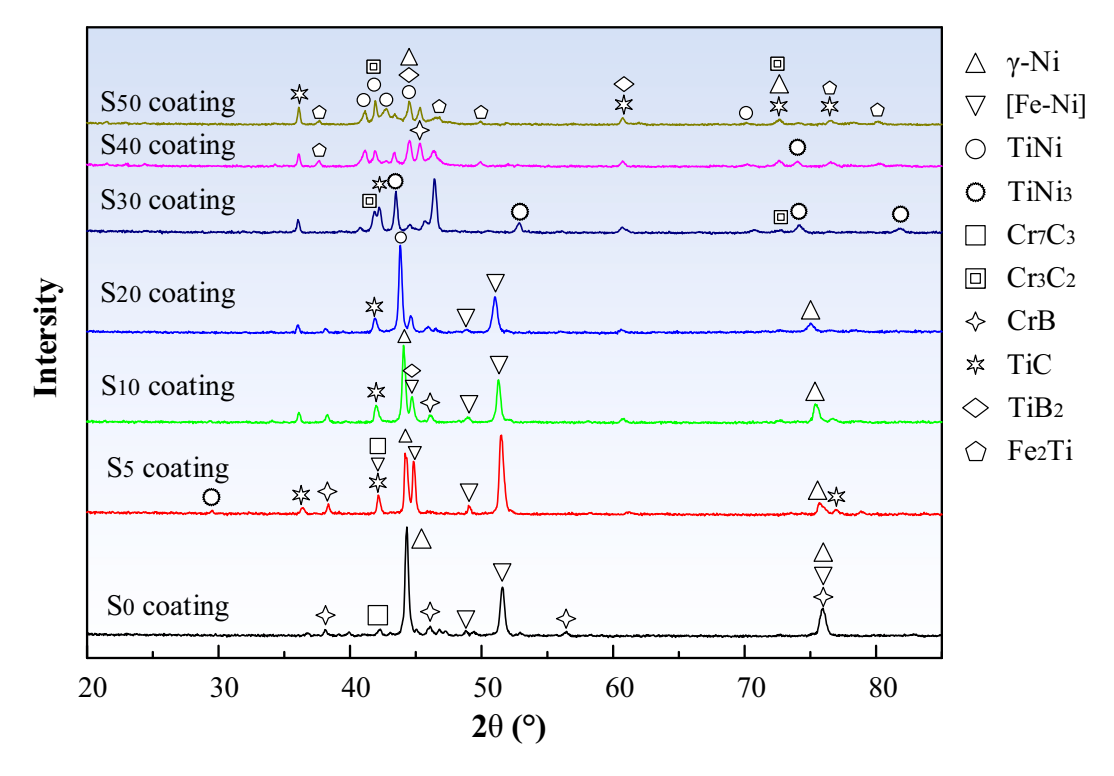


Fig. 3. Comparison among the XRD patterns of NMC coatings fabricated with increasing Ti + C wt%.

samples were ultrasonically cleaned in alcohol for 2 min before testing. Phase compositions were analyzed on plane 1 through an X-ray diffractometer (XRD, X Pertpro, Netherlands, Cu-Ka radiation) with 20 range from 20° to 90°. The microstructure of the NMC coatings was detected by SEM with EDS on plane 2. The cross-sectional microhardness was taken along the building direction on plane 2 using a Vickers indentation tester (HV-1000, Shanghai) with a load of 300 g load and dwell time of 10 s at an interval of 300 µm. The scratch and wear tests were carried out on plane 1 using the material surface property tester (MFT-4000) to comprehensively evaluate the wear performance. Reciprocating friction tests were carried out on plane 1 using an Al₂O₃ ball with a diameter of 8 mm (hardness >90 HRC) at room temperature. The detailed parameters are a normal load of 15 N, a track length of 3.0 mm, a speed of 220 mm/min, and a time of 40 min. The 2D and 3D worn surfaces were obtained by laser confocal microscopy (OLS4000, Japan). Since the wear loss is quite small compared to the mass of samples, the measurement error of the volume loss by laser confocal microscopy

would be greatly reduced owing to its high measurement accuracy and powerful data processing capabilities. In addition, to ensure the credibility of the data, all tests were carried out at least twice, and the average value was taken in this study.

3. Results and analysis

3.1. Phase analysis

Fig. 3 indicates XRD patterns of seven NMC coatings with different Ti + C content. The main diffraction peaks show that the phases are γ -Ni, [Fe–Cr] solid solution, CrB, TiC, TiB₂, TiNi, Ti₃Ni, and Fe₂Ti according to Joint Committee on Powder Diffraction Standards (JCPDS). During the LDED process, there were the following reactions according to XRD results.

$$Ti + 2B \rightarrow TiB_2 \tag{1}$$

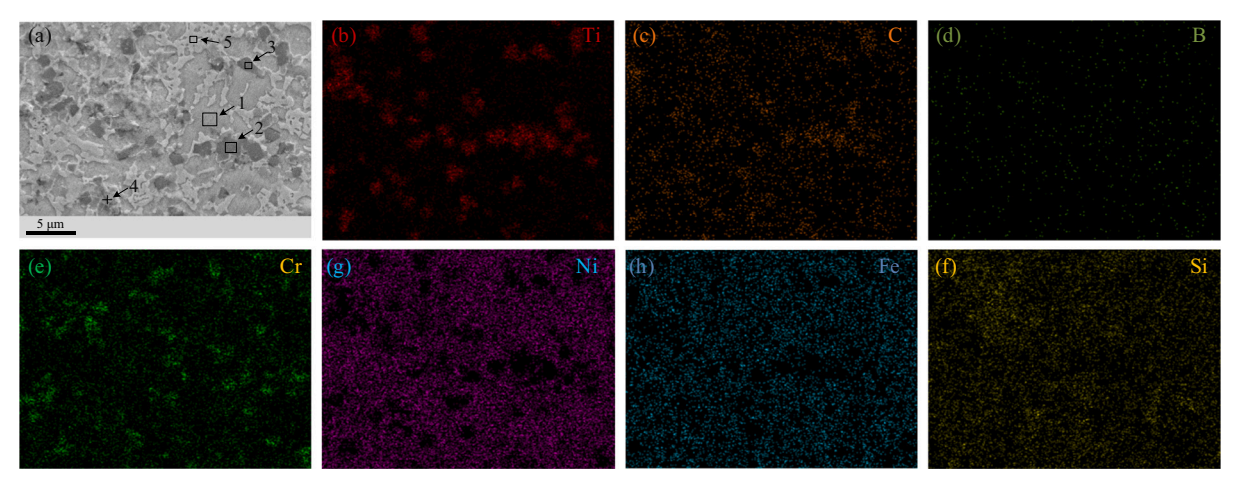


Fig. 4. The distribution of Ti, C, B, Cr, Ni, Fe, and Si elements in S5 coating.

Table 2
Elemental composition (at. %) of various phases from EDS results in Figs. 4, 5, and 6.

Coating	Area	Ti	С	В	Cr	Si	Fe	Ni	Possible phase
S5	1	43.39	44.5	4.13	5.18	0.39	0.43	1.98	TiC
	2	48.29	44.68	2.16	2.88	0.32	0.12	1.55	TiC
	3	1.08	28.25	20.51	23.22	1.52	5.20	20.22	CrB
	4	1.37	7.80	0.00	17.88	5.07	9.46	58.42	Cr ₇ C ₃
	5	1.37	7.80	0.00	7.88	5.07	9.46	68.42	γ -Ni + [Fe-Ni]
S30	6	24.83	14.07	0.00	6.09	3.45	4.92	46.64	TiNi ₂
	7	2.73	6.25	0.00	8.60	3.90	19.73	58.79	[Fe-Ni]
	8	46.23	45.93	4.97	1.25	0.15	0.40	1.07	TiC
	9	40.28	44.49	13.69	0.82	0.00	0.00	0.72	TiC
	10	26.79	12.10	55.76	2.10	0.21	0.38	2.66	TiB_2
	11	1.80	21.56	5.33	40.12	0.79	6.40	24.0	Cr ₇ C ₃
S50	12	2.56	21.69	4.85	30.94	0.73	6.26	32.97	Cr ₃ C ₂
	13	38.7	4.94	0.00	5.01	2.08	3.64	45.63	TiNi
	14	37.02	6.18	4.31	2.13	5.85	14.05	30.46	Fe ₂ Ti
	15	45.86	41.13	12.06	0.30	0.00	0.00	0.65	TiC
	16	46.74	48.57	0.00	1.97	0.53	2.14	0.05	TiC
	17	28.23	16.13	48.13	2.25	0.43	1.15	3.68	TiB ₂
	18	45.45	24.29	28.37	0.70	0.00	0.00	1.19	TiC+TiB ₂
	19	25.4	11.70	54.23	1.81	0.39	2.40	4.07	TiB_2

$$Ti + C \rightarrow TiC$$
 (2)
 $Ti + B \rightarrow TiB$ (3)

$$7Cr + 3C \rightarrow Cr_7C_3 \tag{4}$$

$$3Cr + 2C \rightarrow Cr_3C_2 \tag{5}$$

$$Ti + Ni \rightarrow TiNi$$
 (6)

$$2\mathbf{F}\mathbf{e} + \mathbf{T}\mathbf{i} \rightarrow \mathbf{F}\mathbf{e}_2\mathbf{T}\mathbf{i} \tag{7}$$

The results confirmed that S0 coating was confirmed as $\gamma-Ni, \ [Fe-Ni]$ solid solution, CrB, and Cr7C3 phases by JCPDS 00–003–1043, JCPDS 00–026–0790, JCPDS 98–003–0603, and JCPDS 00–036–1482, respectively, which is consistent with our previous study [15]. One should note that some new peaks corresponding to TiC (JCPDS 03–065–8805), TiB2 (JCPDS 00–035–0741), Cr3C2 (JCPDS 03-065-0897), TiNi3 (JCPDS 01–075–0878), TiNi (JCPDS 98–016–6370), and Fe2Ti (JCPDS 98–063–3956) are detected with Ti + C addition. Meanwhile, as the Ti + C content increased, the intensity of TiC and TiB2 diffraction peaks increased. The matrix was transformed from $\gamma-Ni$ to TiNi3 and finally to TiNi with the enhancement of the Ti element. In addition, the Fe element was consumed to form intermetallic Fe2Ti instead of [Fe-Ni] solid solution. Moreover, the CrB phases are only found in S0, S5, S10, and S20 coatings. However, in S30, S40, and S50 coatings, the B element was

only detected in TiB₂, indicating that the increase in Ti content promoted the transition from CrB to TiB₂. Moreover, the peak intensity of TiC at 35.95° , 60.53° , and 72.45° is also increased with the increase of Ti + C content. According to XRD results, as the Ti + C content increases from 0 wt% to 50 wt%, the phases in the NMC coating first changes from γ –Ni, [Fe–Ni] solid solution, CrB, Cr $_{7}$ C $_{3}$ to [Fe–Ni] solid solution, CrB, Cr $_{7}$ C $_{3}$, TiNi $_{2}$ TiC, TiB $_{2}$ and finally to TiNi, Cr $_{3}$ C $_{2}$, Fe $_{2}$ Ti, TiC, TiB $_{2}$.

The S5 coating mainly consisted of four types of microstructures according to the elemental mapping, as shown in Fig. 4. As one reinforcement, the smaller-sized gray granular particles are the enrichment of Ti and C elements (Fig. 4b and c). Besides, the atomic ratio of Ti and C is nearly 1:1 according to EDS results (Area 2 and 3), as listed in Table 2. This indicates that TiC particles are situ synthesized in S5 coating combined with the XRD results. The second type of long strip shape reinforcements (Area 4) is composited of Cr and B elements. Moreover, the atomic ratio of Cr to B is nearly 1:1, confirming the CrB phases. As shown in Fig. 4c and e, the light gray phases are rich in Cr and C elements, implying that these are Cr_7C_3 based on the EDS result of Area 5. In addition, the matrix phase mainly contains Ni and Fe elements, which indicates that the matrix is composed of γ -Ni and [Fe-Ni] solid solutions.

Fig. 5 indicates that the phase morphologies and the corresponding element distribution in S30 coating fabricated with 30 wt% Ti + C particles changed significantly. Compared with Figs. 4b and 5b, the concentration of Ti element in S30 coating increased significantly,

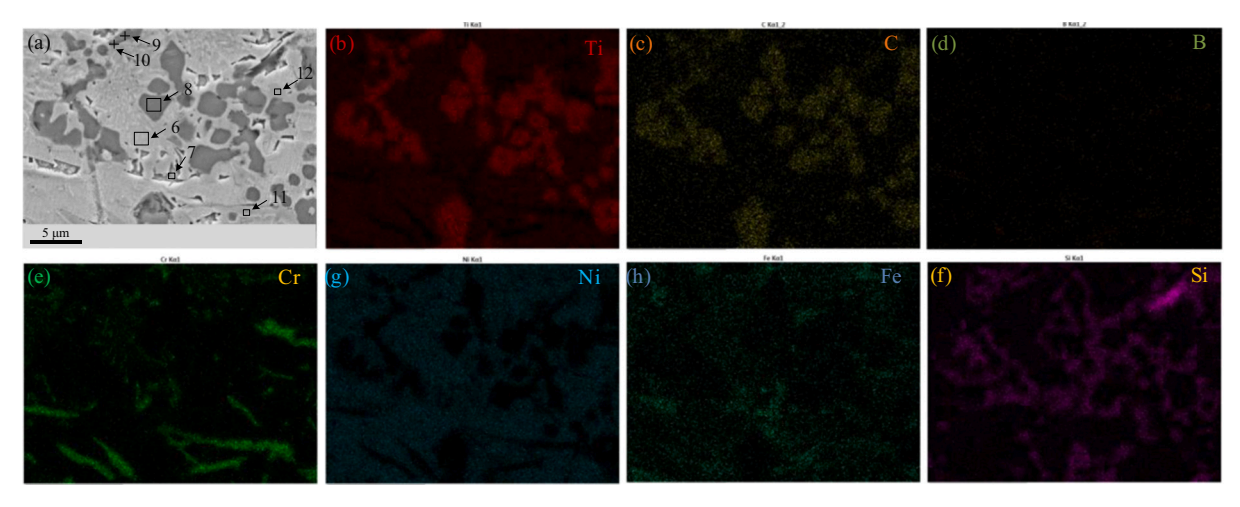


Fig. 5. The distribution of Ti, C, B, Cr, Ni, Fe, and Si elements in S30 coating.

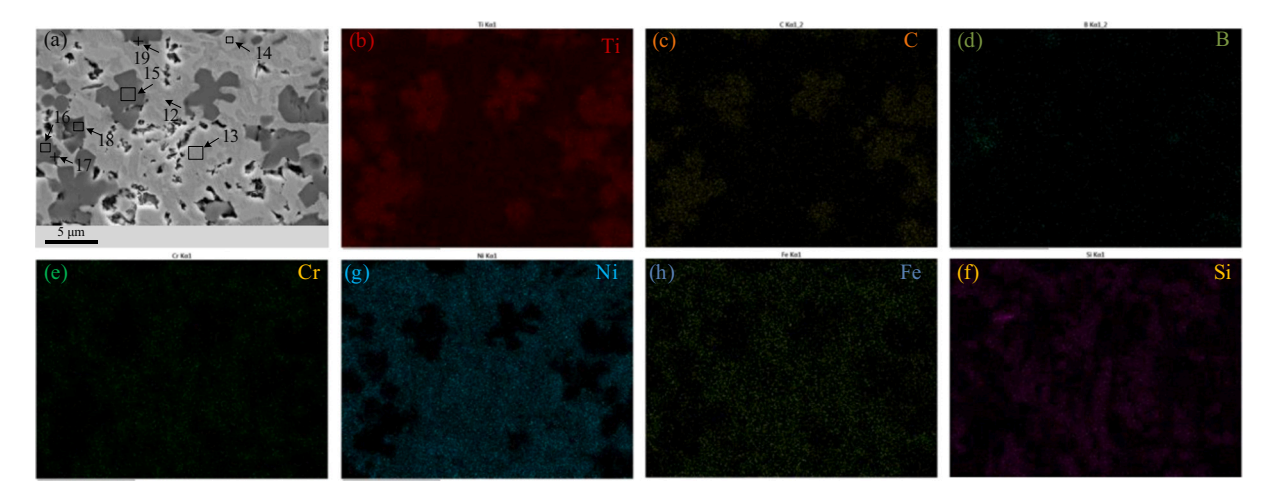


Fig. 6. The distribution of Ti, C, B, Cr, Ni, Fe, and Si elements in S50 coating.

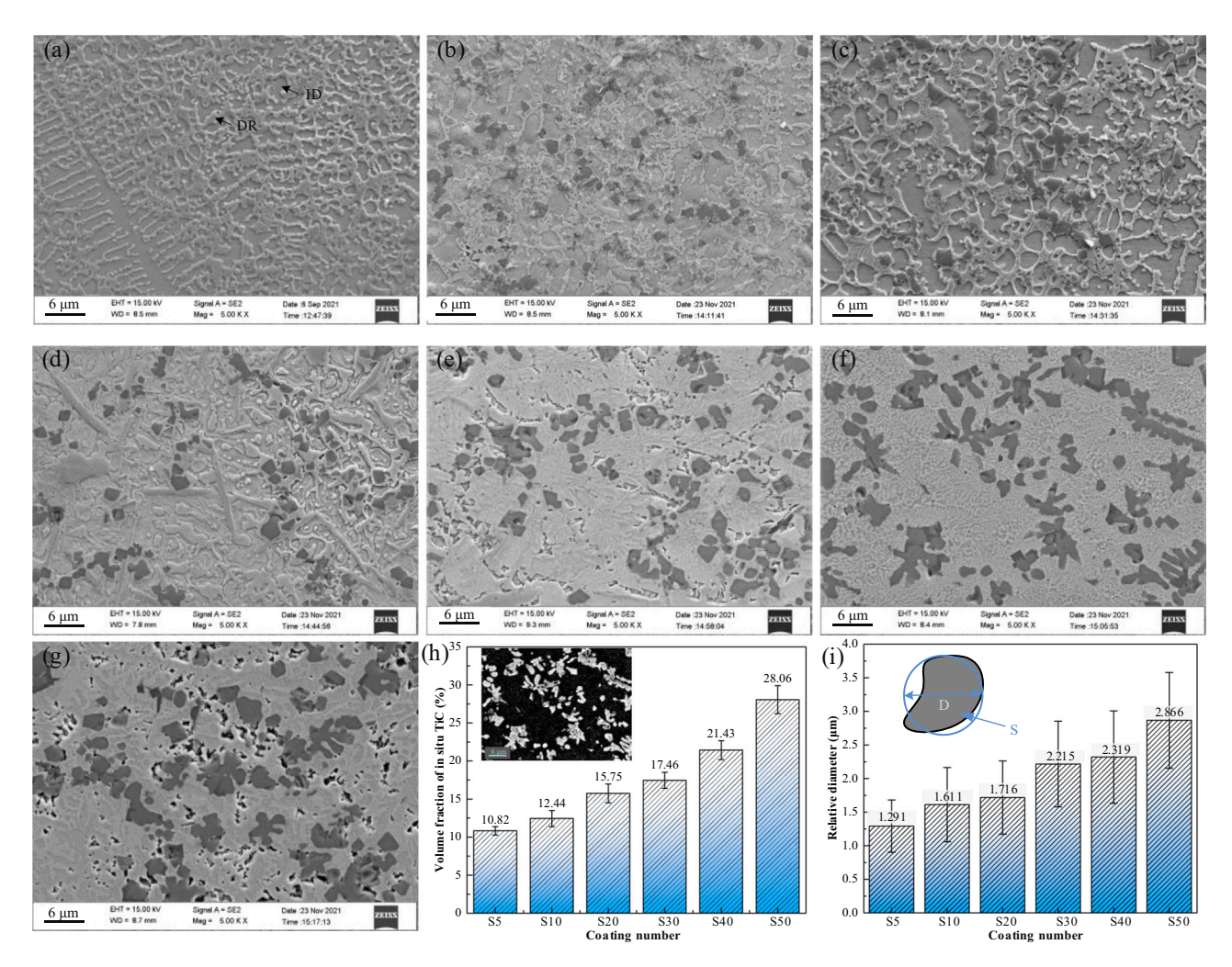


Fig. 7. SEM images of (a) S0 coating, (b) S5 coating (c) S10 coating, (d) S20 coating, (e) S30 coating, (f) S40 coating and (g) S50 coating, (h) and (i) volume fraction and relative diameter of in situ TiC.

which also can be confirmed by EDS results in Areas 5 and 6. The matrix is proved to contain TiNi $_3$. Area 7 is rich in Fe and Ni elements, indicating that [Fe–Ni] solid solution was finally solidified. Literature [30,33] has proved that the two competing factors influence reaction spontaneously: Gibbs free energy (ΔG) and solute concentration. Lower ΔG of Cr_3C_7 and increasing concentration of C element promoted the

transformation from CrB to Cr_7C_3 [34]. Therefore, the size and number of identified Cr_3C_7 (Areas 11 and 12) have been increased, as shown in Fig. 5e. However, the B elements are liable to combine with Ti elements to form the strongest compound TiB₂ (Area 10) among all Ti–B compounds [35]. Additionally, TiC particles are surrounded by a net microstructure composed of Si elements, as shown in Fig. 5a and f. Sun

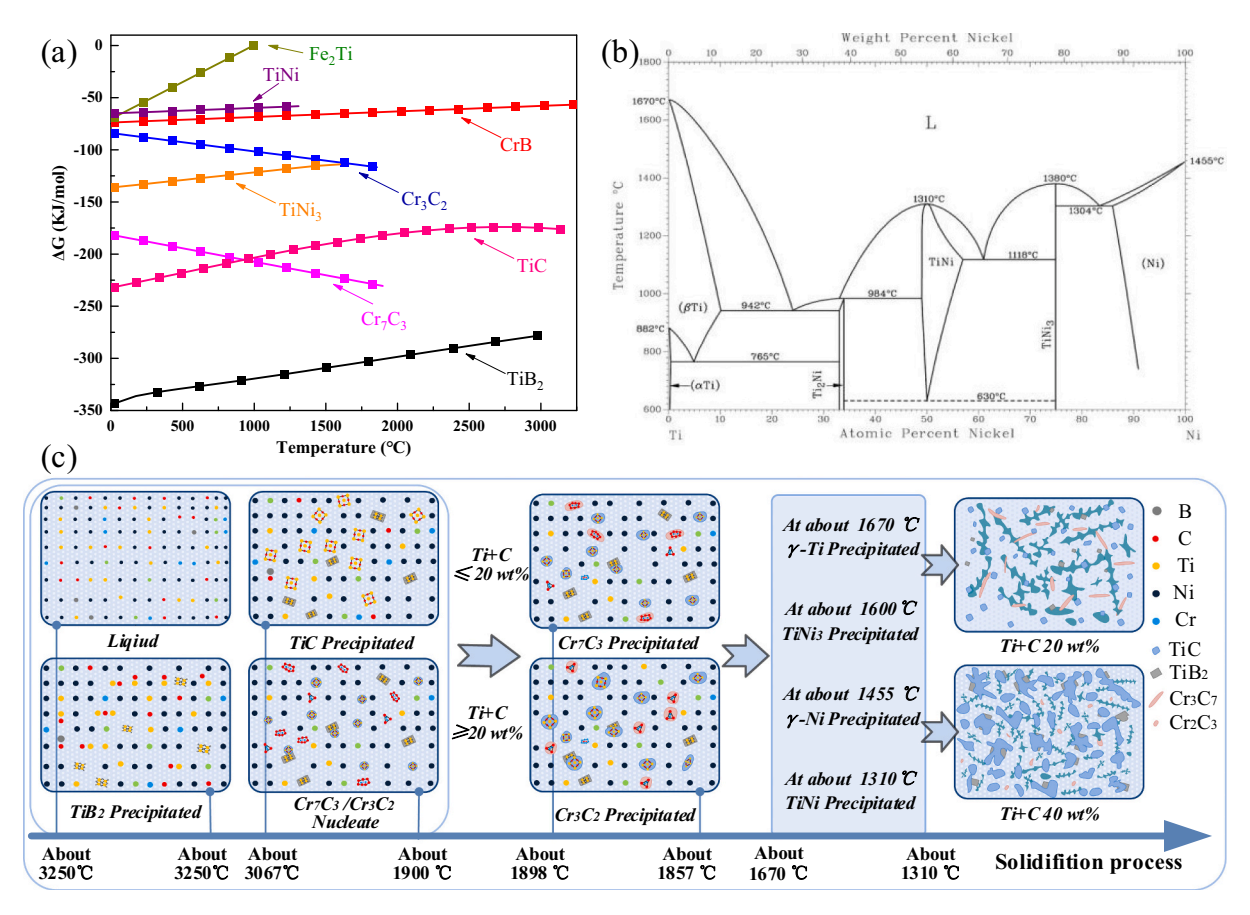


Fig. 8. (a) Gibbs free energy of main reactions during solidification process [34,38,49], (b) Ti–Ni binary system [39]. (c) Schematic diagram showing the effect of Ti + C content on the solidification process of composites.

et al. [36] pointed out that the Si element could promote the liquid flow and further refine the solidified phases, which is beneficial to improving wear resistance.

When Ti + C content reaches 50 wt%, phase characterization in S50 coating is shown in Fig. 6a. The big flower-shaped particles (Area 15 and 16) are proved to be TiC by the XRD and EDS results. The small blockshaped black reinforcements can be regarded as TiB2 according to EDS results of Area 17 and 19. Interestingly, note that all TiB2 particles are only found on the edge of TiC. This phenomenon is not similar to previous studies [37,38]. Liang [39] pointed out that TiB2 would prefer to precipitate due to the lowest ΔG in Ti–C–B system. The formation of TiB₂ consumed the B element near the solidification front and thus increased the concentration of the C element. Therefore, although B atoms were not completely consumed, TiC began to rapidly grow due to the high ratio of Ti to C. This behavior inhibits the growth of TiB2. As shown in Fig. 6a, the white phase is rich with Fe and Ni elements and can be ascribed to Fe₂Ti according to the EDS result of Area 14. In the last stage of the solidification process, a large number of remaining Ti elements are combined with Ni elements to generate the intermetallic compound of TiNi (Area 13).

3.2. Microstructural characterization

The SEM images of NMC coatings fabricated with different Ti + C content are shown in Fig. 7. As shown, the effect of Ti + C content on the microstructure is visible. Image processing software (Image-Pro Plus 6.0) was employed to obtain the volume fraction and relative diameter $(D = L \text{ (Circumference)}/\pi)$ of TiC particles, and the results are shown in Fig. 7h and (i). Fig. 7a portrays that S0 coating is composited of a large number of dendritic (DR) structures and inter-dendritic (ID) matrix, which has been verified as Cr(C, B) and γ -Ni based on our study [15].

The D and volume fraction of fine TiC in the grain boundary of S5 coating are 1.291 \pm 0.389 μm and 10.82 \pm 0.108 %, respectively. Meanwhile, the size of DR structures in S5 coating is significantly decreased due to fine grain strengthening of TiC. With the addition of Ti + C particles up to 10 wt%, the increment of the C element provided the required mass source for the Cr₇C₃. Therefore, the DR structure becomes significantly coarser. This phenomenon is more significant in S20 coating, where the D and volume fraction of TiC particles are 1.716 \pm $0.545\,\mu m$ and 15.75 ± 0.158 %. Interestingly, when the content of Ti +C particles is beyond 30 %, the grains in S30, S40, and S50 coatings are refined. The corresponding D are 2.215 \pm 0.638 μ m, 2.319 \pm 0.687 μ m, and 2.866 \pm 0.711 μ m, which all exceed 2.00 μ m. Capaldi et al. [40] and Gopinath et al. [21] found that the reaction $(2^{\#})$ between Ti and C elements could release a lot of heat. The increase in absolute temperature can weaken the surface tension according to the finding by Sahoo et al. [41]. This phenomenon could promote the expansion of the molten pool and increase the convection velocity. Therefore, the agglomeration of the solute element is reduced, resulting in the dispersed distribution of the reinforcements [30,42]. Additionally, the rich C element promotes the transformation from coarse Cr₇C₃ to fine Cr₃C₂. These reinforcements acted as nucleation sites and refined the microstructure. However, with the Ti + C content further increasing, some unfilled pores were also observed in S40 and S50 coatings, as shown in Fig. 7f and g.

According to XRD, EDS results, and SEM images, a schematic diagram of the solidification process is obtained to deeply reveal the effect of TiC content on the microstructure evolution, as shown in Fig. 8, The precursor with different content of Ti + C particles were melted to form Ni–Ti–Fe–C–B multicomponent liquid under the high energy of laser beam. Besides, strong Marangoni convection (velocity > 200 mm/s) can promote the uniform distribution of these solutes [30]. Fig. 8a indicates that reactions $(1^{\#\#})$ – $(7^{\#\#})$ could take place, spontaneously because the

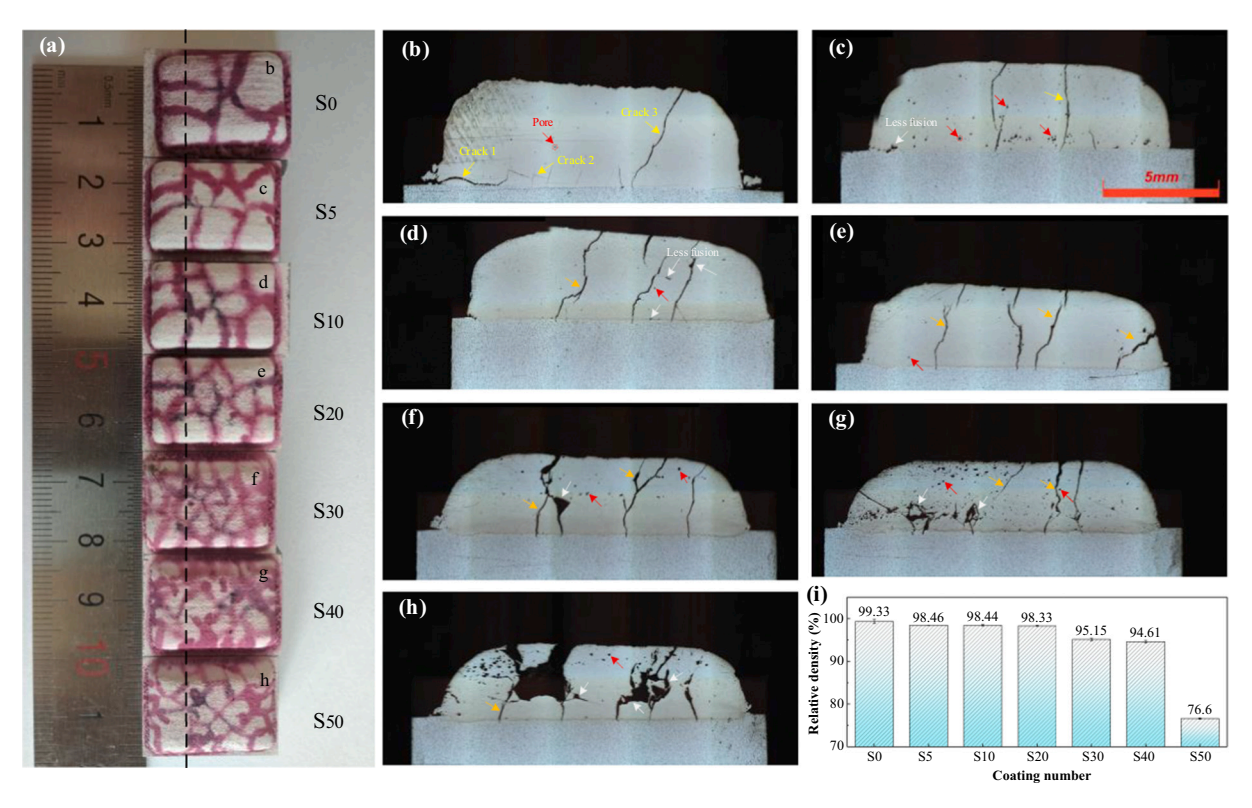


Fig. 9. (a) The overall morphologies of specimens; optical images showing the cross–sectional photograph: (b) S0 coating, (c) S5 coating (d) S10 coating, (e) S20 coating, (f) S30 coating, (g) S40 coating, (h) S50 coating, and (i) relative density.

 ΔG of all reactions is negative when the temperature is below the corresponding melting point. At the beginning of solidification, when the temperature exceeds 3250 °C, TiB2 would be preferentially nucleated because of the lowest ΔG and most robust crystal structure in the Ti-C-B system [43], as shown in Fig. 8c. The tiny TiB₂ with a typical hexagonal crystal structure would be rapidly grown along with the (0001) orientation by alternating layers of Ti and B elements. Therefore, the solidified TiB2 remains in equilibrium morphology as hexagonal platelet, which was confirmed by Chi et al. [44] and Zhang et al. [45]. When the temperature drops to 3067 °C, TiC began to grow as a shape of granular or dendrite because of its crystalline structure of NaCl-type, and orientation of (0001). Ogwu et al. [46] found the eutectic temperature between TiB₂ and TiC to be 2620 \pm 5 °C. Besides, precipitated preferentially TiB2 could serve as heterogeneous nucleation sites for TiC because the disregistry between TiC (111) and TiB₂ (0001) is near 1.0 %. This value is far less than the most effective heterogeneous nucleation (6.0 %) reported by Chi [44] and Tang [47]. Therefore, TiB₂ phases are only generated on the edge of TiC to form TiB2/TiC composites in the consideration of limited B elements. When it came to the eutectic temperature of Cr_7C_3 at about 1900 °C, Cr_7C_3 with smaller ΔG began to nucleate and grow preferentially (Fig. 8a). Meanwhile, when the content of Ti + C particles is <30 %, rich Cr elements are easier to combine with C elements to solidify into a large strip of Cr_3C_7 with a length $> 5 \ \mu m$ owing to the high surface energy, as shown in Figs. 5e and 7d. These coarse compounds could weaken the toughness and improve the probability of peeling off of the reinforcements [48]. Notably, when the content of Ti + C particles is >20 wt%, rich C elements improve the nucleation sites of Cr-C compounds. Besides, all Cr elements are almost consumed to generate fine Cr₂C₃ in the cause of the increase of C/Cr ratio in S30, S40, and S50 coatings. Therefore, the solute concentration plays an increasingly dominant role rather than ΔG with the increase of Ti + C content. Therefore, coarse Cr₇C₃ is transformed into fine Cr₂C₃. According to Fig. 8b, TiNi3 was generated in S5, S10, and S20 coatings at about 1600 °C due to a higher Ni/Ti ratio and smaller ΔG . While, with

the increase of Ti + C content, TiNi formed at about 1310 °C according to the reaction: $L+\text{TiN}_3\to\text{TiNi}$ at the last stage of the solidification process (Figs. 6a and 7g). Therefore, NMC coatings fabricated with Ti + C content $<\!30$ wt% are composed of fine TiC reinforcements (D<1.8 μm) and coarse matrix. While, S30, S40, and S50 coatings are composited of coarse TiC reinforcements ($D>2.2~\mu\text{m}$) and fine matrix, as shown in Fig. 8c.

3.3. Crack and porosity

The crack sensitivities were investigated via penetrant flaw detection on the surface of the NMC coating, and the results are depicted in Fig. 9a. As the increase of Ti + C content, the surface crack rate is gradually increased. However, the crack size is gradually reduced. This phenomenon suggests that crack extension can be inhibited by coarse TiC particles, where D is >2.2 µm. According to Fig. 9b-h, cracks characterization can be classified into transverse and longitudinal according to their orientation. Based on the liquid film strain concentration theory [33,50], intergranular liquid film and sufficient tensile stress are the two prerequisites for cracking. A transverse crack originates on the side of the SO coating, extends horizontally to the interior, and displays an irregular zigzag pattern. The previous research [3,22] has found that the residual stress in AM metal composites is primarily tensile stress rather than structural stress during the rapid melting and solidification process. The squeezing of the solution by the pre-deposited track results in the shrinkage of the compression deformed region being less than that on the free compression deformed surface. Therefore, the residual tensile stresses are formed in the lapping region. The uniformly distributed TiC particles with low thermal conductivity weaken the temperature gradient (G) and expansion of thermal stress, resulting in less crack propagation. As shown in Fig. 9c-h, longitudinal cracks from the surface to the bottom are throughout the NMC coatings. The crack characteristics are very similar to the previous studies [31,50,51]. As the laser beam moves away, the heat exchange between the coating surface

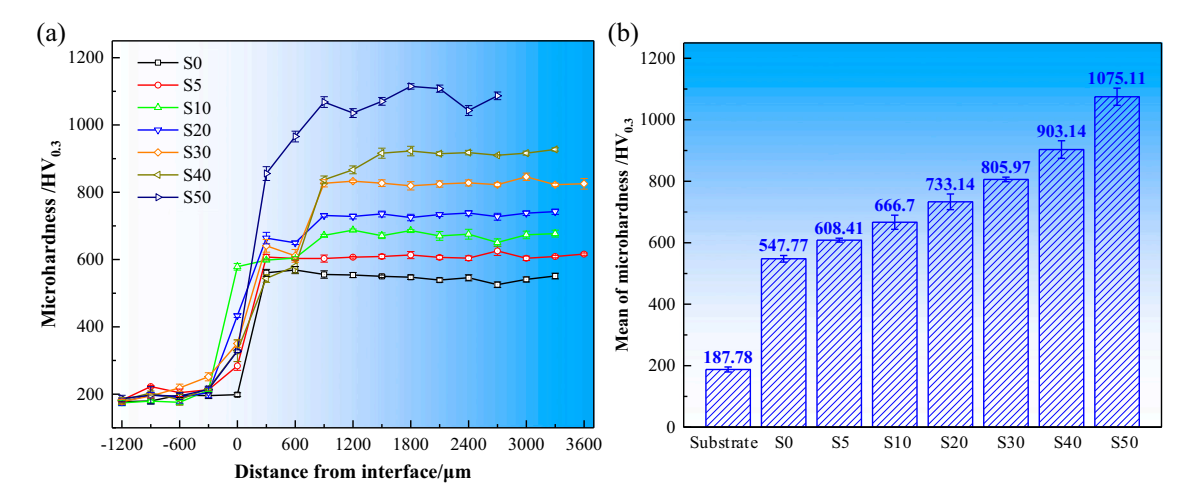


Fig. 10. (a) Microhardness distribution along building direction, and (b) average microhardness of each coating.

and the cold air increases the cooling rate. Therefore, large thermal/ shrinkage stress promotes crack generation on the coating surface. Besides, the coarse columnar grains with a strong orientation of (001) are usually generated near the bonding zone between the coating and substrate. Low melting eutectics (like $\gamma + \gamma'$) and carbides in the interdendritic region of columnar grain boundaries accelerated crack expansion. Meanwhile, the brittleness of the composite coating was increased by the lack of a corresponding slip system for ceramic materials. Therefore, some penetration cracks are generated when Ti + C content is <40 wt%. Besides, porosity is another defect to be avoided because it not only reduces the densification but also can be regarded as a source of crack The oxidation of the Ni-coated C particles or the cavitation of the material results in the regular spherical pores [37]. Moreover, coarse ceramic particles can inhibit the flow of liquids, resulting in the formation of irregular pores, as shown in Fig. 9g and h. The relative density of NMC coatings was measured by the Archimedes method, and the results are shown in Fig. 9i. The densification of NMC coatings decreases with the increase of Ti + C content. As the content of reinforcements increases, the viscosity of the liquid becomes higher, decreasing the flowability. The spherification trend of the micro melt driven by the surface tension would be increased. As a result, more unfilled regions are found in the S30, S40, and S50 coatings.

3.4. Microhardness

Fig. 10 elucidates the microhardness of NMC coatings along the building direction and their average values as well. The microhardness increases from 187.78 \pm 8.19 HV $_{0.3}$ in the substrate to high microhardness values with gradients depending on TiC content. The average microhardness of S0 coating is 547.77 \pm 10.93 HV_{0.3}, which is consistent with the previous study [15]. Fig. 10b indicates that the microhardness of the NMC coating is proportional to the content of Ti + C particles. The microhardness of S5 coating is 608.41 \pm 0.3 HV_{0.3}, which is 60.64 HV_{0.3} higher than that of S0 coating. As the volume fraction of the reinforcements increased from a minimum of 10.82 % in S5 coating to a maximum of 28.06 % in S50 coating, the microhardness was increased from 608.41 \pm 6.25 HV_{0.3} to a maximum of 1075.11 \pm 27.94 $HV_{0.3}$. The S50 coating exhibits the highest microhardness, which is 5.73 and 1.96 times that of the substrate and S0 coating, respectively. On the one hand, rich C elements not only combined with Ti to form TiC particles but also reacted with Cr elements to generate carbides, such as Cr₃C₇ and Cr₂C₃. On the other hand, Ti promoted the generation of reinforcements including TiB2, TiNi, and Fe2Ti. The in situ synthesized reinforcements with sequential precipitation could act as nucleation sites and refine the grain, as deliberated earlier in Fig. 8. Therefore, the deformability of NMC coating could be improved by fine-grained strengthening [27,52,53]. Besides, fine reinforcements can be easily

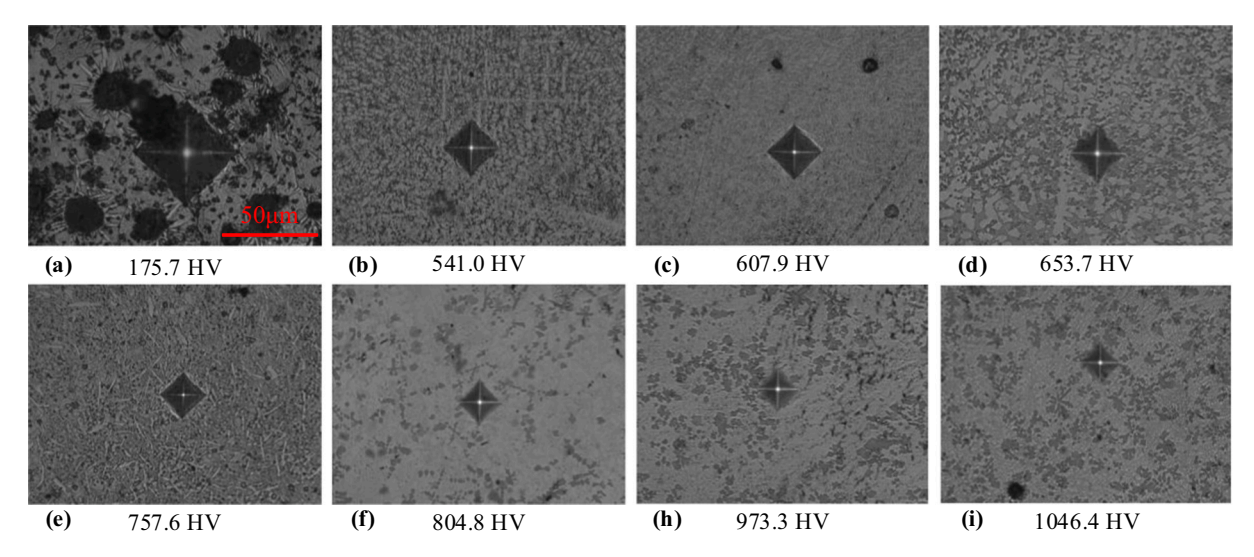


Fig. 11. Indentation images: (a) substrate, (b) S0 coating, (c) S5 coating (d) S10 coating, (e) S20 coating, (f) S30 coating, (g) S40 coating and (h) S50 coating.

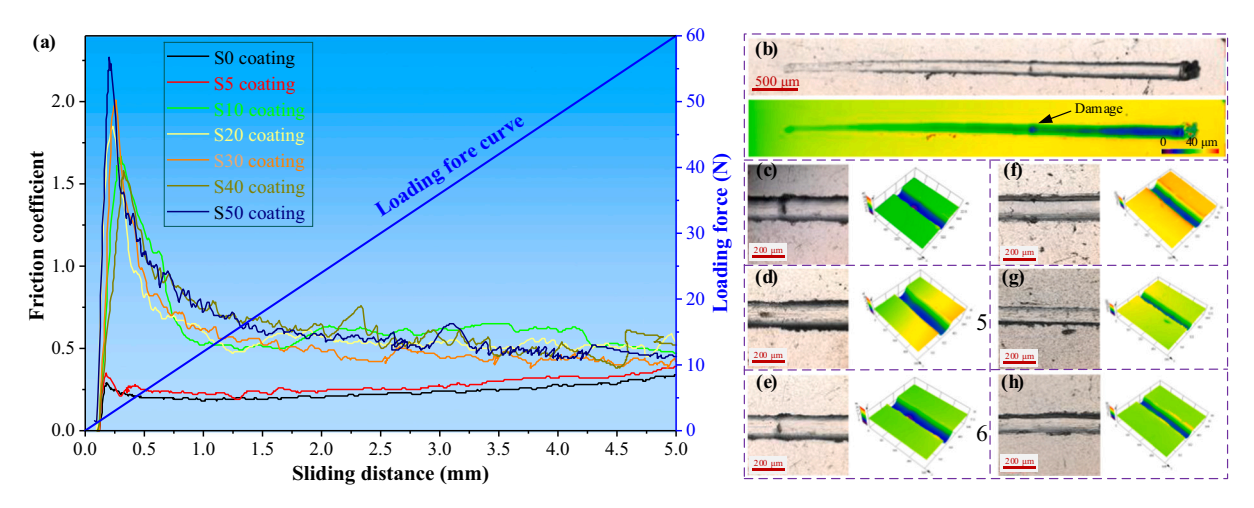


Fig. 12. Effect of loading force on friction coefficient of different coating: (a) test result, (b) surface morphology of S5 coating, (c-h): critical failure location of S5-S50 coatings.

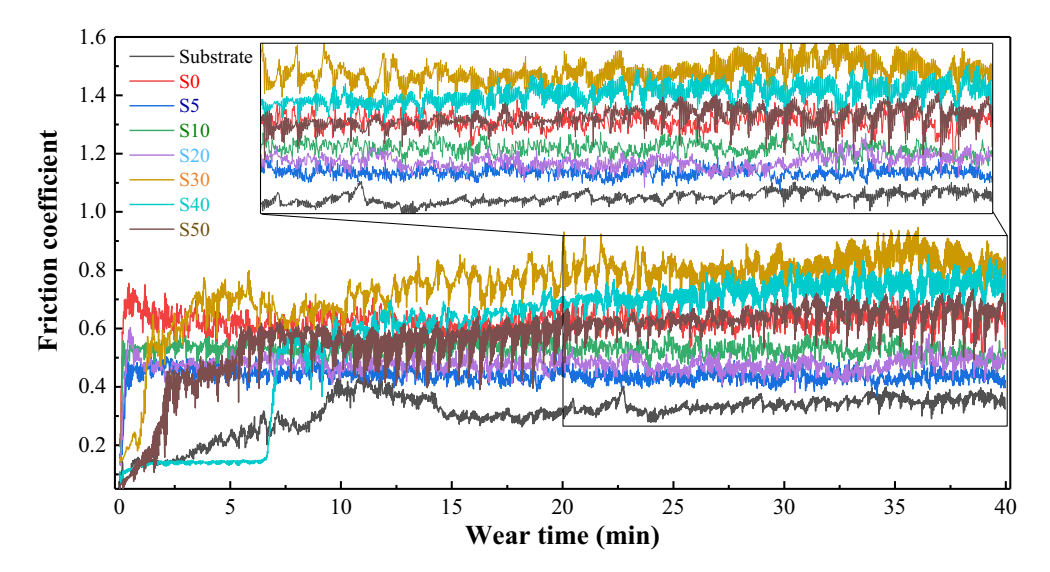


Fig. 13. COF vs. time curves of different coating.

diffused into the matrix, which increases the resistance to deformation [54,55]. As the literature [4,15,56] reported, the aggregation of reinforcements in NMC coatings fabricated with directly added hard particles is very serious because of the density variations and the strong convection. However, in this study, the microhardness distribution of NMC coating is very uniform in both the building and lapping directions. This is attributed to finer grains, the smaller size of reinforcements, and the more uniform microstructure. Fig. 11 demonstrates some representative indications performed on NMC coatings with different TiC content. No micro-cracks are observed at the edges of the indentation, which characters that the ductility remains good toughness despite its reasonably high microhardness [43,57].

3.5. Wear resistance

The wear resistance of TiC reinforced composites is evaluated via friction coefficient, wear volume, and worn surfaces in this study. To assess the deformation resistance and coefficient of friction (COF) under progressively increasing loads, the scratching needle (diamond indenter with 90°) was loaded on the plane 1 from 0 N to 60 N at a loading speed of 100 N/min, where the sliding distance is 6.0 mm. Fig. 12a illustrates the variation in the COF vs. loading force. The S0 coatings represent a

lower COF. As the load force increase, the COF of the S5–S50 coating first increases to a maximum value, then gradually decreases to be stable. The variation in COF indicates that the resistance to plastic deformation of composite coatings with increasing TiC content was increased significantly. Besides, Fig. 12c shows the optical and depth images of the whole scratch morphology of the S5 coating. Due to poor resistance to deformation, the surface S5 coating was damaged during the scratching process, as the loading force gradually increased. Similar damages were also found in the S10 and S20 coatings, as shown in Fig. 12d–f. Interestingly, the damages are not observed in S30, S40, and S50 coating, where the volume fraction and size of reinforcements are >17 % and 2.2 μm , respectively. In addition, with the increase of TiC content, the plastic deformation at the edge of the scratch track is gradually reduced, as represented in Fig. 12g–h.

Fig. 13 represents the COFs curves of NMC coatings fabricated with different Ti + C particles. The wear process can be divided into the swearing-in stage and the stable wearing stage according to the fluctuation of COFs. The previous research [27,49] has found that abrasive wear and adhesive wear are the removal mechanisms of particles-reinforced composites. Therefore, surface fluctuations allow for occlusion between the Al_2O_3 ball and coating material at the swearing-in stage. As some materials were removed, the contact area between the

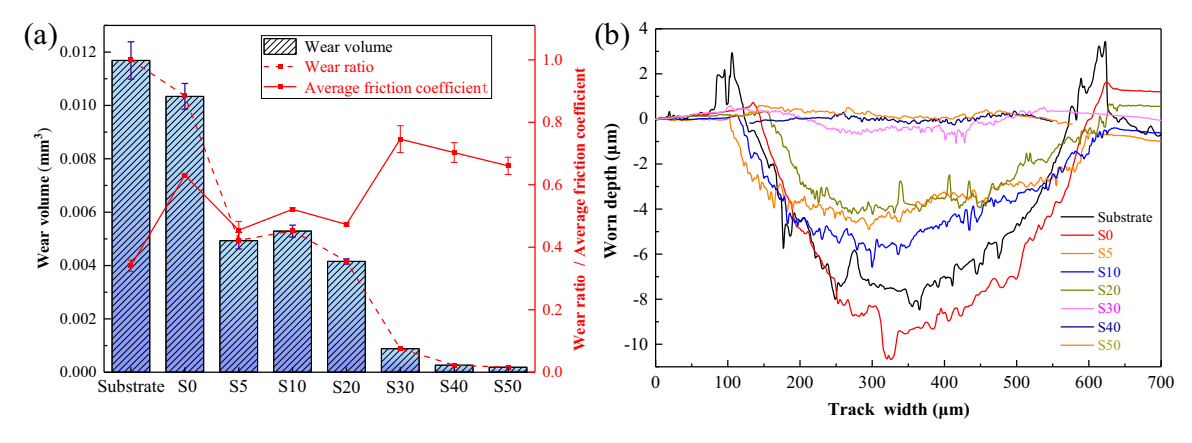


Fig. 14. (a) The COF and volume loss, and (b) the wear cross-section profiles of coatings.

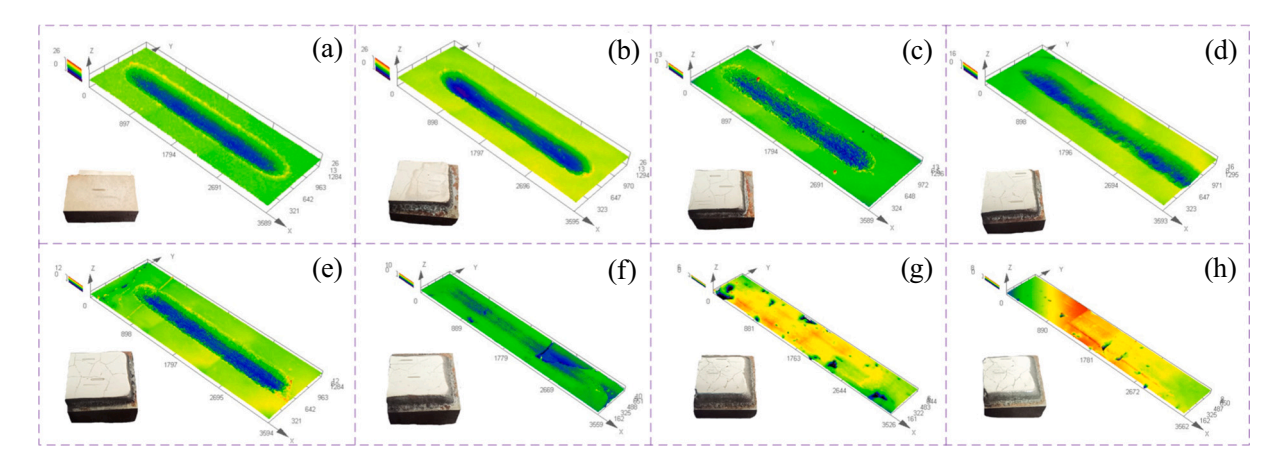


Fig. 15. 3D worn track: (a) substrate, (b) S0 coating, (c) S5 coating (d) S10 coating, (e) S20 coating, (f) S30 coating, (g) S40 coating and (h) S50 coating.

 $\rm Al_2O_3$ ball and the coatings becomes larger, so the COF tended to be smooth in the last 20 min. Therefore, the average COF of NMC coating was obtained within a wear time of 20–40 min, as shown in Fig. 14a. The COFs of S5, S10, and S20 coatings are 0.45, 0.52, and 0.47, respectively, which is significantly lower than that of S0 coating (0.63). Interestingly, the COFs of S30, S40, and S50 coatings are significantly increased when the volume fraction of TiC is $>\!17$ %, indicating a stronger resistance to deformation.

Fig. 15 represents the 3D worn surfaces of NMC coatings fabricated with different Ti + C wt%. The larger edge deformation and deeper scratches are observed in the substrate and S0 coating due to low microhardness. As the volume fraction of in situ TiC increases from 10.32 % to 28.06 %, the depth of the wear track is reduced. Besides, the worn surface is smoother. The relative removal rate (i.e. ratio of the volume loss of NMC coating to that of the substrate) is defined in this study, and the results are shown in Fig. 14a. As TiC content increases, the volume removal decreases from 103.401 \times 10⁻³ to 0.184 \times 10⁻³ mm³, as shown in Fig. 14a. Interestingly, compared to the other coatings, volume removal of S30, S40 and S50 coatings is significantly lower despite their large COFs. This suggests that the content of in situ TiC has a significant impact on the wear mechanism. To deep reveal the characteristics of the wear track, cross-section profiles were obtained and shown in Fig. 14b. The wear tracks of the substrate, S0, S5, S10, and S20 coatings are deep and wide, and the wear depth is $>4 \mu m$, corresponding to relatively severe wear. With the increase of in situ TiC content, the depth of the wear track decrease. Moreover, when the content of Ti + C particles is >30 wt%, the wear depth is <1.0 µm. The above analysis indicates that the wear resistance of the NMC coating can be effectively improved only when the volume fraction and relative diameter of reinforcements are >17.0 % and 2.2 $\mu m,$ respectively.

To reveal the effect of in situ TiC content on wear mechanisms, 2D worn surfaces are obtained, as shown in Fig. 16. It is noted that microcracks are not found in all coatings from enlarged views, suggesting that these coatings have good toughness. As shown in Fig. 16a and b, deep valleys and some spalling are found on the worn surface of substrate and S0 coating. A large number of pits are observed on the worn surface of S5, S10, and S20 coatings. These coatings tend to undergo large plastic deformation during the wear process. In addition, local residual stresses in LDED NMC coatings increase the crack sensitiveness, and then micro-cracks tend to be generated [33,58]. As the Al₂O₃ ball repeatedly slides on the coating surface, the materials near the contact point are eventually sheared off due to the propagation of microcracks. As the wear test proceeds, the flaking materials were transferred to the surface of the grinding ball or debris. Therefore, some pits and grooves are generated on worn surfaces when the volume fraction and relative diameter of reinforcements are ${<}15.75$ % and 1.716 ${\mu}m.$ This can be indicated as a typical characteristic of adhesive wear. Fig. 16f shows that the shallow grooves and bulges along the sliding direction are alternately distributed on the worn surface of S30 coating with a volume fraction of 17.46 % and a relative diameter of 2.22 μm . Besides, volume loss is reduced because of the inhibition of coarse reinforcements on the bulges (Fig. 14a). This is related to the characterization of abrasive wear. As shown in Fig. 16g and h, fewer pits and more smooth zones can be found on the worn surfaces of S40 and S50 coating. On the one hand, during the wear process, a large number of uniformly distributed coarse TiC and TiB₂ particles acted as a skeleton to bear the load, preventing the removal of the matrix. On the other hand, the bonding force between the in situ synthesized particles and the matrix is significantly larger than

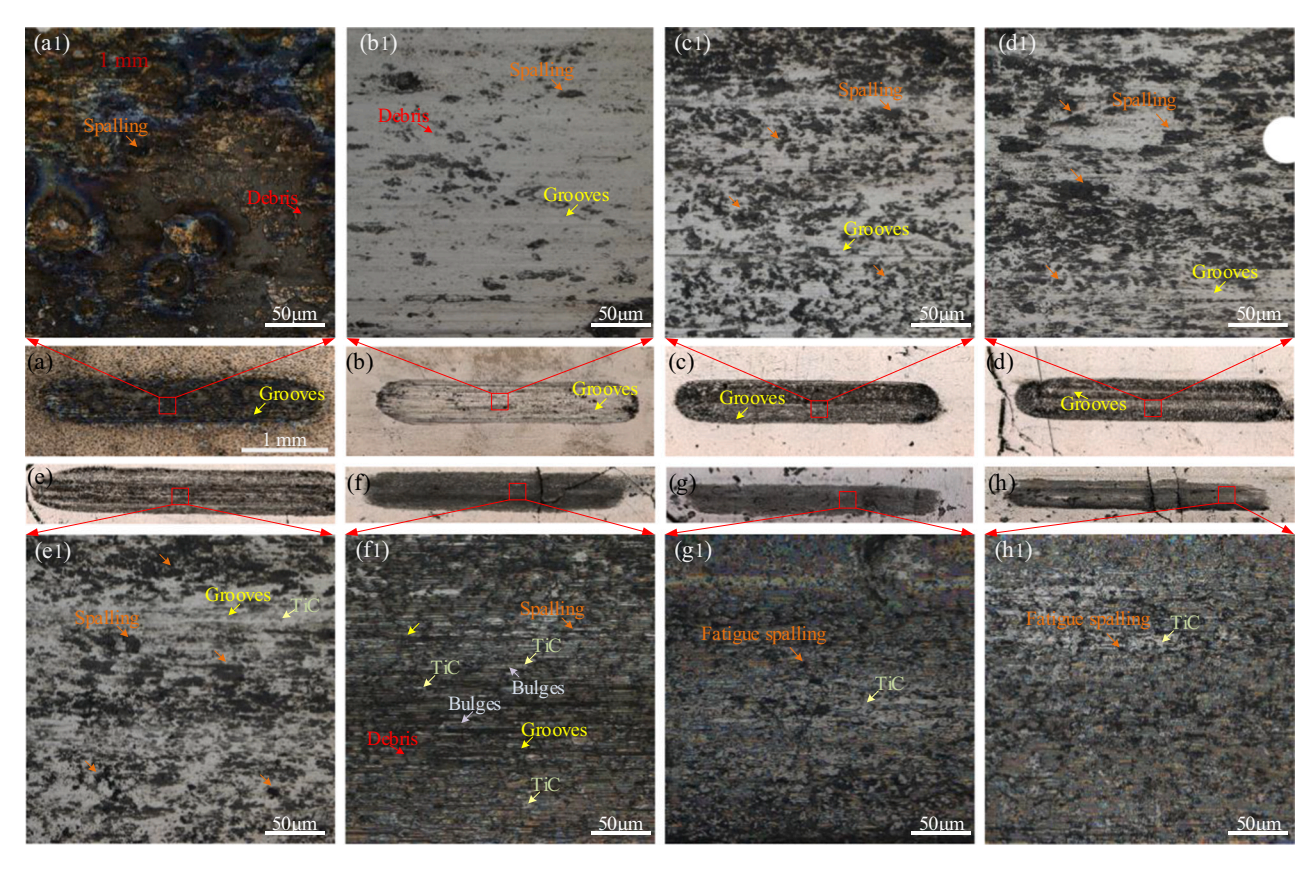


Fig. 16. Optical image of 2D worn surface: (a) substrate, (b) S0 coating, (c) S5 coating (d) S10 coating, (e) S20 coating, (f) S30 coating, (g) S40 coating, and (h) S50 coating.

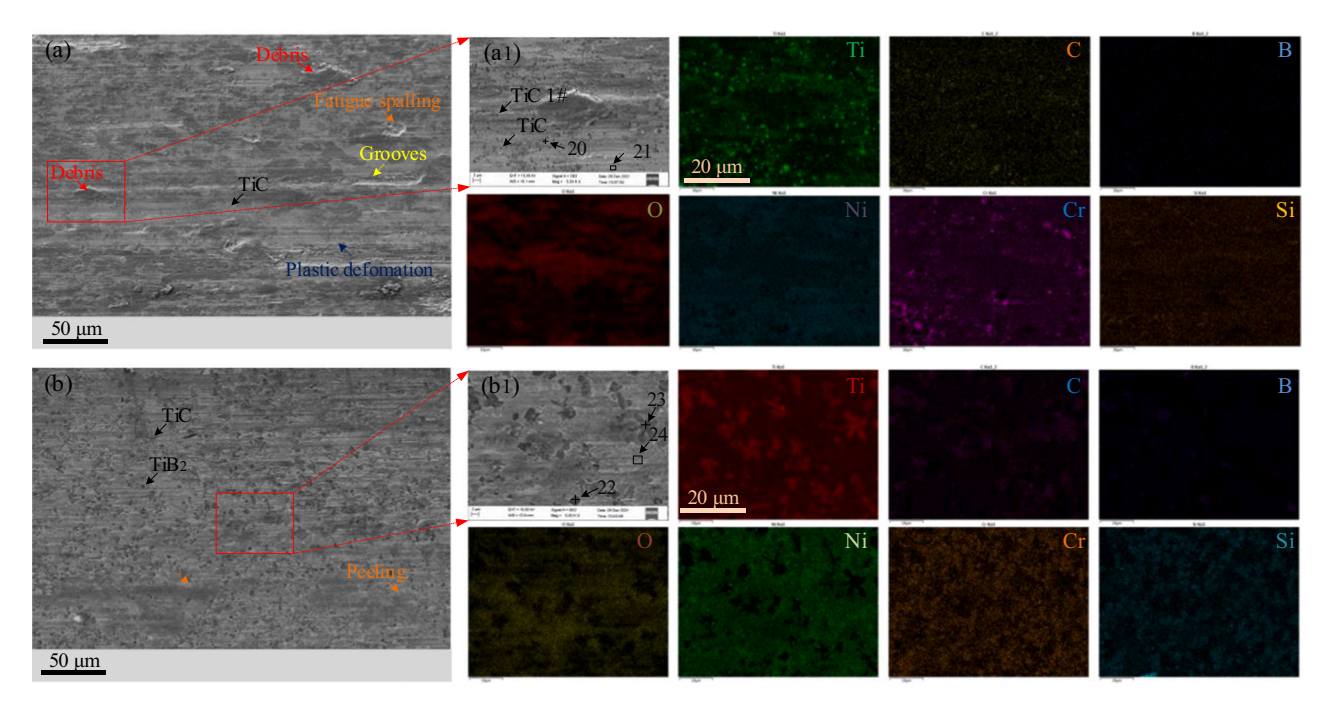


Fig. 17. SEM images of 2D worn surface for (a) S10 coating and (b) S40 coating.

that between the ex-situ particles. Therefore, the spalling of the reinforcements is effectively decreased, resulting in a smoother worn surface with no grooves [15,27,59]. The S40 and S50 coatings with higher microhardness have less plastic deformation during the wear process, resulting in high contact compressive stresses. As a result, small

pits or craters due to flaking off of material are found on the surface of the S40 and S50 coating under multiple stress cycles. Therefore, the S40 and S50 coatings are subject to characteristics of fatigue wear combined with the above analysis.

To reveal the effect of content and size of in situ synthesized TiC on

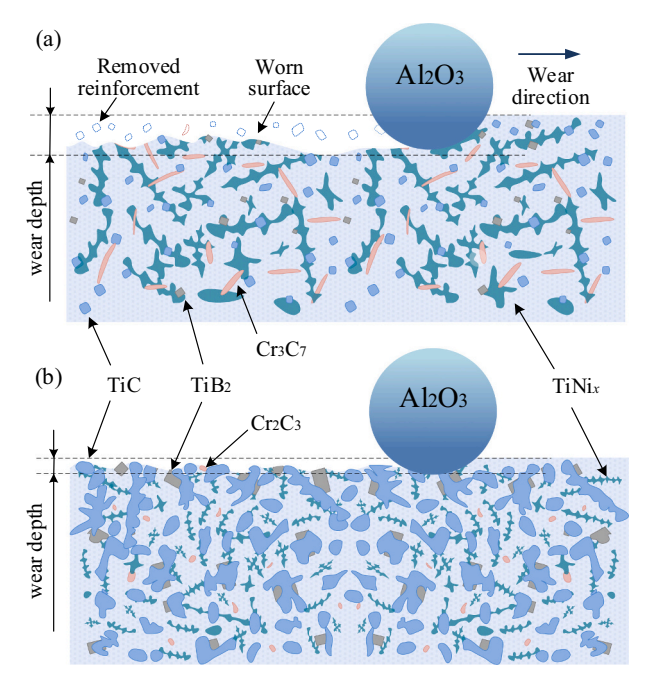


Fig. 18. The schematic diagram of the effect of TiC content on the wear process.

the wear mechanism in detail, the SEM images and schematic diagrams were obtained, as shown in Figs. 17 and 18. As shown in Fig. 17a1, the diffusely distributed gray particles can be identified as in situ synthesized TiC according to EDS results (Table 3). Interestingly, these fine TiC particles are not only distributed in the matrix, but also on the debris. Because the relative diameter ($<1 \mu m$) of fine TiC particles is small enough to be embedded in the microscopic cutting interface, these particles (TiC 1# in Fig. 7a1) are wrapped in the chips and then removed during the wear process, as shown in Fig. 18a. Zum [60] also reported that when the carbide size is <1 μm , the wear resistance decreases with the carbide content increasing. Therefore, significant plastic deformation and severe spalling are found on the worn surface of the S10 coating. As shown in Fig. 17b, the coarse TiC particles with $D > 2.2 \mu m$ are evenly distributed on the worn surface of the S40 coating, and no large gray bands are observed. In addition, some fish-scale morphologies are generated due to the creeping of the material, indicating high microhardness and good resistance to deformation. Moreover, the size of in situ TiC particles is larger than that of the micro-cutting wear interface, thereby, the wear depth is significantly reduced, as shown in Fig. 18b.

4. Conclusions

In this study, a series of NMC coatings containing different TiC content were fabricated with different Ti + C wt% particles by laser

direct energy deposition process. The effect of content and size of in situ synthesized TiC on phases, microstructural evolution, defects, microhardness, and wear resistance were carefully examined and discussed in detail. The new findings and conclusions show that:

- 1. With the increase of Ti+C content in the composite powder, the matrix of the NMC coatings first changes from γ –Ni, [Fe–Ni] solid solution to [Fe–Ni] solid solution and TiNi2, and finally to TiNi due to the increase in Ti/Ni ratio. Besides, the increase in the C/Cr ratio promotes the transition from coarse striped $Cr_{\gamma}C_{3}$ into fine reticulated $Cr_{2}C_{3}$. The phase transition is mainly the result of competing elemental concentration ratios and Gibbs free energy.
- 2. The content and size of TiC particles were effectively governed by Ti + C wt% in the composite powder. As the Ti + C content increases from 5 wt% to 50 wt%, the volume fraction and relative diameter of the in situ synthesized TiC particles are increased from 10.82 % to 28.06 %, and 1.291 μm to 2.866 μm , respectively.
- 3. The transverse and longitudinal cracks are found in NMC coatings, which limits the real application of the composite coatings. With the content of in situ TiC increasing, the crack size decreases because the in situ coarse TiC particles could inhibit the expansion of cracks. This phenomenon is more obvious especially when the relative diameter of TiC is >2.2 μ m. Besides, the increase in volume fraction of TiC reduces the densification.
- 4. As the Ti + C content was increased from 5 wt% to 50 wt%, the microhardness of NMC coatings is increased from a minimum value of 608.41 \pm 6.25 HV0.3 to a maximum of 1075.11 \pm 27.94 HV0.3. The remarkable increment in microhardness is a synergistic effect of fine-grain strengthening, solid solution strengthening, and second phase strengthening.
- 5. The scratch tests indicate that damages are not found on the surface of NMC coatings fabricated with Ti + C particles over 30 wt% because of good resistance to plastic deformation. During the wear test, the volume loss of NMC coatings decreases from 103.401×10^{-3} to 0.184×10^{-3} mm 3 with the increase of in situ TiC content. The relative diameter of TiC particles in the S30 coating is $>\!2.2~\mu\text{m}$, which is large enough to be difficult to be embedded in the microscopic cutting interface. The wear resistance of NMC coatings was significantly improved. As the content of in situ synthesized TiC particles increase, the wear mechanism of the NMC coatings was transformed from adhesive wear to abrasive wear and finally to fatigue wear.

CRediT authorship contribution statement

Liaoyuan Chen: Problem formulation, Conducting of experimentation, Testing, analysis of the results, Writing - review & editing.

Yu Zhao: Problem analysis, Conducting of experimentation, Validation.

Fanwei Meng: Conducting of experimentation, Data curation.

Tianbiao Yu: Supervision, Discussion on the idea, Analysis of the results, Writing-review & editing, Funding acquisition.

Table 3The elemental composition of various phases from EDS results in Fig. 17.

Coatings	Area		Ti	С	В	Cr	Si	Fe	0	Ni	Possible phase
S10	20	wt.%	56.53	18.44	5.60	3.61	0.60	1.12	5.00	9.08	TiC
		at.%	30.97	40.27	13.59	1.82	0.56	0.53	8.2	4.06	
	21	wt.%	7.96	4.96	2.78	8.49	2.71	7.33	4.83	60.94	[Fe-Ni]
		at.%	6.47	16.08	10.02	6.36	3.76	5.11	11.77	40.43	
S40	22	wt.%	50.74	2.66	21.26	3.84	4.19	11.95	3.43	1.92	TiB_2
		at.%	30.95	8.64	55.88	1.88	3.80	5.44	10.45	0.83	
	23	wt.%	70.28	12.09	3.75	2.27	2.64	3.72	4.40	0.84	TiC
		at.%	44.28	30.36	10.45	1.32	2.84	2.01	8.31	0.43	
	24	wt.%	30.47	4.73	2.28	3.37	0.58	2.34	19.17	37.06	NiTi
		at.%	19.91	12.29	6.60	2.03	0.65	1.31	37.47	19.74	

Zhelun Ma: Investigation, Visualization. **Sheng Qu**: Writing - review & editing.

Zhengyu Sun: Conducting of experimentation, Validation.

Declaration of competing interest

The authors declare that they have no known competing financial interests or personal relationships that could have appeared to influence the work reported in this paper.

Data availability

Data will be made available on request.

Acknowledgment

This work was supported by the Fundamental Research Funds for the Central Universities (N2103004); the National Natural Science Foundation of China (52075088).

References

- [1] L. Zhu, Z. Yang, B. Xin, S. Wang, G. Meng, J. Ning, P. Xue, Microstructure and mechanical properties of parts formed by ultrasonic vibration-assisted laser cladding of Inconel 718, Surf. Coat.Technol. 410 (2021), 126964, https://doi.org/ 10.1016/j.surfcoat.2021.126964.
- [2] N. Shamsaei, A. Yadollahi, L. Bian, S.M. Thompson, An overview of direct laser deposition for additive manufacturing; part II: mechanical behavior, process parameter optimization and control, Addit. Manuf. 8 (2015) 12–35, https://doi. org/10.1016/j.addma.2015.07.002.
- [3] T. DebRoy, H.L. Wei, J.S. Zuback, T. Mukherjee, J.W. Elmer, J.O. Milewski, A. M. Beese, A. Wilson-Heid, A. De, W. Zhang, Additive manufacturing of metallic components process, structure and properties, Prog. Mater. Sci. 92 (2018) 112–224, https://doi.org/10.1016/j.pmatsci.2017.10.001.
- [4] Y. Zhao, T. Zhang, L. Chen, T. Yu, J. Sun, C. Guan, Microstructure and mechanical properties of Ti–C–TiN-reinforced Ni204-based laser-cladding composite coating, Ceram. Int. 47 (2021) 5918–5928, https://doi.org/10.1016/j. ceramit 2020.11.054
- [5] T.E. Abioye, P.K. Farayibi, D.G. McCartney, A.T. Clare, Effect of carbide dissolution on the corrosion performance of tungsten carbide reinforced Inconel 625 wire laser coating, J. Mater. Process. Technol. 231 (2016) 89–99, https://doi.org/10.1016/j. jmatprotec.2015.12.023.
- [6] M. Moradi, A. Hasani, Z. Pourmand, J. Lawrence, Direct laser metal deposition additive manufacturing of Inconel 718 superalloy: statistical modelling and optimization by design of experiments, Opt. Laser Technol. 144 (2021), 107380, https://doi.org/10.1016/j.optlastec.2021.107380.
- [7] Y. Zhao, L. Chen, J. Sun, W. Wu, T. Yu, Microstructure evolution and wear resistance of in-situ synthesized (Ti, Nb)C ceramic reinforced Ni204 composite coatings, Ceram. Int. (2022), https://doi.org/10.1016/j.ceramint.2022.03.016.
- [8] R. Saeedi, R. Shoja Razavi, S.R. Bakhshi, M. Erfanmanesh, A. Ahmadi Bani, Optimization and characterization of laser cladding of NiCr and NiCr-TiC composite coatings on AISI 420 stainless steel, Ceram. Int. 47 (2021) 4097–4110, https://doi.org/10.1016/j.ceramint.2020.09.284.
- [9] Z. Tong, H. Liu, J. Jiao, W. Zhou, Y. Yang, X. Ren, Laser additive manufacturing of CrMnFeCoNi high entropy alloy: microstructural evolution, high-temperature oxidation behavior and mechanism, Opt. Laser Technol. 130 (2020), 106326, https://doi.org/10.1016/j.optlastec.2020.106326.
- [10] L. Chen, Y. Zhao, B. Song, T. Yu, Z. Liu, Modeling and simulation of 3D geometry prediction and dynamic solidification behavior of Fe-based coatings by laser cladding, Opt. Laser Technol. 139 (2021), 107009, https://doi.org/10.1016/j. optlastec.2021.107009.
- [11] D. Svetlizky, M. Das, B. Zheng, A.L. Vyatskikh, S. Bose, A. Bandyopadhyay, J. M. Schoenung, E.J. Lavernia, N. Eliaz, Directed energy deposition (DED) additive manufacturing: physical characteristics, defects, challenges and applications, Mater. Today 49 (2021) 271–295, https://doi.org/10.1016/j.mattod.2021.03.020.
- [12] B. Song, T. Yu, X. Jiang, W. Xi, X. Lin, Z. Ma, Z. Wang, Development of the molten pool and solidification characterization in single bead multilayer direct energy deposition, Addit. Manuf. 49 (2022), 102479, https://doi.org/10.1016/j. addma.2021.102479.
- [13] C. Hong, D. Gu, D. Dai, M. Alkhayat, W. Urban, P. Yuan, S. Cao, A. Gasser, A. Weisheit, I. Kelbassa, M. Zhong, R. Poprawe, Laser additive manufacturing of ultrafine TiC particle reinforced Inconel 625 based composite parts: tailored microstructures and enhanced performance, Mater. Sci. Eng. A 635 (2015) 118–128, https://doi.org/10.1016/j.msea.2015.03.043.
- [14] D. Svetlizky, B. Zheng, A. Vyatskikh, M. Das, S. Bose, A. Bandyopadhyay, J. M. Schoenung, E.J. Lavernia, N. Eliaz, Laser-based directed energy deposition (DED-LB) of advanced materials, Mater. Sci. Eng. A 840 (2022), 142967, https://doi.org/10.1016/j.msea.2022.142967.

- [15] L. Chen, Y. Zhao, X. Chen, T. Yu, P. Xu, Repair of spline shaft by laser-cladding coarse TiC reinforced ni-based coating: process, microstructure and properties, Ceram. Int. 47 (2021) 30113–30128, https://doi.org/10.1016/j. ceramint 2021 07 189
- [16] R. Fathi, H. Wei, B. Saleh, N. Radhika, J. Jiang, A. Ma, M.H. Ahmed, Q. Li, K. K. Ostrikov, Past and present of functionally graded coatings: advancements and future challenges, Appl. Mater. Today 26 (2022), 101373, https://doi.org/10.1016/j.apmt.2022.101373.
- [17] Y. Zhao, T. Yu, J. Sun, S. Jiang, Microstructure and properties of laser cladded B4C/TiC/Ni-based composite coating, Int. J. Refract. Met. Hard Mater. 86 (2020), 105112, https://doi.org/10.1016/j.ijrmhm.2019.105112.
- [18] G. Muvvala, S. Mullick, A.K. Nath, Development of process maps based on molten pool thermal history during laser cladding of Inconel 718/TiC metal matrix composite coatings, Surf. Coat.Technol. 399 (2020), https://doi.org/10.1016/j. surfcoat.2020.126100.
- [19] S. Saroj, C.K. Sahoo, M. Masanta, Microstructure and mechanical performance of TiC-Inconel825 composite coating deposited on AISI 304 steel by TIG cladding process, J. Mater. Process. Technol. 249 (2017) 490–501, https://doi.org/ 10.1016/j.jmatprotec.2017.06.042.
- [20] L. Chen, T. Yu, X. Chen, Y. Zhao, C. Guan, Process optimization, microstructure and microhardness of coaxial laser cladding TiC reinforced Ni-based composite coatings, Opt. Laser Technol. 152 (2022), 108129, https://doi.org/10.1016/j. optlastec.2022.108129.
- [21] G. Muvvala, D. Patra Karmakar, A.K. Nath, In-process detection of microstructural changes in laser cladding of in-situ Inconel 718/TiC metal matrix composite coating, J. Alloys Compd. 740 (2018) 545–558, https://doi.org/10.1016/j. iallcom.2017.12.364.
- [22] Z. Ma, Q. Wang, H. Chen, L. Chen, S. Qu, Z. Wang, T. Yu, A grinding force predictive model and experimental validation for the laser-assisted grinding (LAG) process of zirconia ceramic, J. Mater. Process. Technol. 302 (2022), https://doi. org/10.1016/j.jmatprotec.2022.117492.
- [23] Y. Sun, L. Jin, Y. Gong, X. Wen, G. Yin, Q. Wen, B. Tang, Experimental evaluation of surface generation and force time-varying characteristics of curvilinear grooved micro end mills fabricated by EDM, J. Manuf. Process. 73 (2022) 799–814, https:// doi.org/10.1016/j.jmapro.2021.11.049.
- [24] C. Cui, Z. Guo, H. Wang, J. Hu, In situ TiC particles reinforced grey cast iron composite fabricated by laser cladding of Ni-Ti-C system, J. Mater. Process. Technol. 183 (2007) 380–385, https://doi.org/10.1016/j.jimatprotec.2006.10.031.
- [25] M.J. Hamedi, M.J. Torkamany, J. Sabbaghzadeh, Effect of pulsed laser parameters on in-situ TiC synthesis in laser surface treatment, Opt. Lasers Eng. 49 (2011) 557–563, https://doi.org/10.1016/j.optlaseng.2010.12.002.
- [26] T. Chen, F. Wu, H. Wang, D. Liu, Laser cladding in-situ Ti(C, N) particles reinforced Ni-based composite coatings modified with CeO2 nanoparticles, Metals (Basel) 8 (2018), https://doi.org/10.3390/met8080601.
- [27] Y. Zhao, T. Yu, L. Chen, Y. Chen, C. Guan, J. Sun, Microstructure and wear resistance behavior of Ti-C-B4C-reinforced composite coating, Ceram. Int. 46 (2020) 25136–25148, https://doi.org/10.1016/j.ceramint.2020.06.300.
- [28] Z. Tong, X. Ren, J. Jiao, W. Zhou, Y. Ren, Y. Ye, E.A. Larson, J. Gu, Laser additive manufacturing of FeCrCoMnNi high-entropy alloy: effect of heat treatment on microstructure, residual stress and mechanical property, J. Alloys Compd. 785 (2019) 1144–1159, https://doi.org/10.1016/j.jallcom.2019.01.213.
- [29] L. Yang, T. Yu, M. Li, Y. Zhao, J. Sun, Microstructure and wear resistance of in-situ synthesized Ti(C, N) ceramic reinforced fe-based coating by laser cladding, Ceram. Int. 44 (2018) 22538–22548, https://doi.org/10.1016/j.ceramint.2018.09.025.
- [30] L. Chen, T. Yu, P. Xu, B. Zhang, In-situ NbC reinforced Fe-based coating by laser cladding: simulation and experiment, Surf. Coat.Technol. 412 (2021), 127027, https://doi.org/10.1016/j.surfcoat.2021.127027.
- [31] L. Chen, Y. Zhao, C. Guan, T. Yu, Effects of CeO2 addition on microstructure and properties of ceramics reinforced Fe-based coatings by laser cladding, Int. J. Adv. Manuf. Technol. 115 (2021) 2581–2593, https://doi.org/10.1007/s00170-021-07297-8.
- [32] Y. Zhao, T. Yu, J. Sun, L. Chen, Y. Chen, Effect of laser cladding on forming microhardness and tensile strength of YCF101 alloy powder in the different full lap joint modes, J. Alloys Compd. 820 (2020), 150230, https://doi.org/10.1016/j. jallcom.2019.04.046.
- [33] S. Chandra, X. Tan, R.L. Narayan, C. Wang, S.B. Tor, G. Seet, A generalised hot cracking criterion for nickel-based superalloys additively manufactured by electron beam melting, Addit. Manuf. 37 (2021), 101633, https://doi.org/10.1016/j. addma.2020.101633.
- [34] Q. Wu, W. Li, N. Zhong, W. Gang, W. Haishan, Microstructure and wear behavior of laser cladding VC-Cr7C3 ceramic coating on steel substrate, Mater. Des. 49 (2013) 10–18, https://doi.org/10.1016/j.matdes.2013.01.067.
- [35] G. Wen, S.B. Li, B.S. Zhang, Z.X. Guo, Reaction synthesis of TiB2-TiC composites with enhanced toughness, Acta Mater. 49 (2001) 1463–1470, https://doi.org/ 10.1016/S1359-6454(01)00034-9.
- [36] W. Su, X. Cui, Y. Yang, Y. Guan, Y. Zhao, S. Wan, J. Li, G. Jin, Effect of Si content on microstructure and tribological properties of Ti5Si3/TiC reinforced NiTi laser cladding coatings, Surf. Coat.Technol. 418 (2021), 127281, https://doi.org/ 10.1016/j.surfcoat.2021.127281.
- [37] D. Tijo, M. Masanta, A.K. Das, In-situ TiC-TiB2 coating on Ti-6Al-4V alloy by tungsten inert gas (TIG) cladding method: part-I.Microstructure evolution, Surf. Coat. Technol. 344 (2018) 541–552, https://doi.org/10.1016/j. surfcoat.2018.03.082.
- [38] Y. Liu, L. Yang, X. Yang, T. Zhang, R. Sun, Optimization of microstructure and properties of composite coatings by laser cladding on titanium alloy, Ceram. Int. 47 (2021) 2230–2243, https://doi.org/10.1016/j.ceramint.2020.09.063.

- [39] J. Liang, X. Yin, Z. Lin, S. Chen, C. Liu, C. Wang, Microstructure and wear behaviors of laser cladding in-situ synthetic (TiBx+TiC)/(Ti2Ni+TiNi) gradient composite coatings, Vacuum 176 (2020), 109305, https://doi.org/10.1016/j. vacuum.2020.109305.
- [40] M.J. Capaldi, A. Saidi, J.V. Wood, Reaction Synthesis of TiC and Fe–TiC Composites 37, ISIJ International, 1997, pp. 188–193.
- [41] P. Sahoo, T. Debroy, M.J. McNallan, Surface tension of binary metal-surface active solute systems under conditions relevant to welding metallurgy, Metall. Trans. B 19 (1988) 483–491, https://doi.org/10.1007/BF02657748.
- [42] P. Yuan, D. Gu, Molten pool behaviour and its physical mechanism during selective laser melting of TiC/AlSi10Mg nanocomposites: simulation and experiments, J. Phys. D. Appl. Phys. 48 (2015), https://doi.org/10.1088/0022-3727/48/3/ 035303.
- [43] Y. Lin, Y. Lei, X. Li, X. Zhi, H. Fu, A study of TiB2/TiB gradient coating by laser cladding on titanium alloy, Opt. Lasers Eng. 82 (2016) 48–55, https://doi.org/ 10.1016/j.optlaseng.2016.01.016.
- [44] Y. Chi, G. Gong, L. Zhao, H. Yu, H. Tian, X. Du, C. Chen, In-situ TiB2-TiC reinforced Fe-Al composite coating on 6061 aluminum alloy by laser surface modification, J. Mater. Process. Technol. 294 (2021), 117107, https://doi.org/10.1016/j. imatprotec.2021.117107.
- [45] M. Zhang, G.L. Zhao, X.H. Wang, S.S. Liu, W.L. Ying, Microstructure evolution and properties of in-situ ceramic particles reinforced Fe-based composite coating produced by ultrasonic vibration assisted laser cladding processing, Surf. Coat. Technol. 403 (2020), 126445, https://doi.org/10.1016/j.surfcoat.2020.126445.
- [46] A.A. Ogwu, T.J. Davies, The densification and mechanical properties of a TiC and TiB2 hardmetal sintered with a reactive alloy binder, Phys. Status Solidi Appl. Res. 153 (1996) 101–116, https://doi.org/10.1002/pssa.2211530109.
- [47] J. Tang, Mechanical and tribological properties of the TiC-TiB2 composite coating deposited on 40Cr-steel by electro spark deposition, Appl. Surf. Sci. 365 (2016) 202–208, https://doi.org/10.1016/j.apsusc.2015.12.198.
- [48] Z. Tong, H. Liu, J. Jiao, W. Zhou, Y. Yang, X. Ren, Improving the strength and ductility of laser directed energy deposited CrMnFeCoNi high-entropy alloy by laser shock peening, Addit. Manuf. 35 (2020), 101417, https://doi.org/10.1016/j. addma.2020.101417.
- [49] L. Chen, T. Yu, C. Guan, Y. Zhao, Microstructure and properties of metal parts remanufactured by laser cladding TiC and TiB2 reinforced Fe-based coatings, Ceram. Int. (2022), https://doi.org/10.1016/j.ceramint.2022.01.299.
- [50] Y.L. Hu, X. Lin, K. Song, X.Y. Jiang, H.O. Yang, W.D. Huang, Effect of heat input on cracking in laser solid formed DZ4125 superalloy, Opt. Laser Technol. 86 (2016) 1–7, https://doi.org/10.1016/j.optlastec.2016.06.008.

- [51] M. Zhang, D. Wang, L. He, X. Ye, W. Ouyang, Z. Xu, W. Zhang, X. Zhou, Microstructure and elevated temperature wear behavior of laser-cladded AlCrFeMnNi high-entropy alloy coating, Opt. Laser Technol. 149 (2022), 107845, https://doi.org/10.1016/j.optlastec.2022.107845.
- [52] D. Tijo, M. Masanta, In-situ TiC-TiB2 coating on Ti-6Al-4V alloy by tungsten inert gas (TIG) cladding method: part-II. Mechanical performance, Surf. Coat.Technol. 344 (2018) 579–589, https://doi.org/10.1016/j.surfcoat.2018.03.083.
- [53] R. Salloom, S.S. Joshi, N.B. Dahotre, S.G. Srinivasan, Laser surface engineering of B4C/Fe nano composite coating on low carbon steel: experimental coupled with computational approach, Mater. Des. 190 (2020), 108576, https://doi.org/ 10.1016/j.matdes.2020.108576.
- [54] S. Zhou, Y. Zhao, X. Wang, W. Li, D. Chen, T.B. Sercombe, Enhanced corrosion resistance of Ti-5 wt.% TiN composite compared to commercial pure Ti produced by selective laser melting in HCl solution, J. Alloys Compd. 820 (2020), 153422, https://doi.org/10.1016/j.jallcom.2019.153422.
- [55] Z. Tong, X. Pan, W. Zhou, Y. Yang, Y.X. Ye, D. Qian, X. Ren, Achieving excellent wear and corrosion properties in laser additive manufactured CrMnFeCoNi highentropy alloy by laser shock peening, Surf. Coat.Technol. 422 (2021), 127504, https://doi.org/10.1016/j.surfcoat.2021.127504
- [56] H. Chen, Y. Lu, Y. Sun, Y. Wei, X. Wang, D. Liu, Coarse TiC particles reinforced H13 steel matrix composites produced by laser cladding, Surf. Coat.Technol. 395 (2020), 125867, https://doi.org/10.1016/j.surfcoat.2020.125867.
- [57] D.T. Waghmare, C. Kumar Padhee, R. Prasad, M. Masanta, NiTi coating on Ti-6Al-4V alloy by TIG cladding process for improvement of wear resistance: microstructure evolution and mechanical performances, J. Mater. Process. Technol. 262 (2018) 551-561, https://doi.org/10.1016/j.jimatprotec.2018.07.033.
- [58] M. Xie, C. Wu, S. Zhou, J. Jin, S. Zhao, D. Chen, TiB2- and Fe2P with nanotwins-reinforced Cu-based immiscible composites fabricated by selective laser melting: formation mechanism and wear behavior, J. Alloys Compd. 864 (2021), 158716, https://doi.org/10.1016/j.jallcom.2021.158716.
- [59] M. Xie, S. Zhou, S. Zhao, J. Jin, D. Chen, L.C. Zhang, In-situ Fe2P reinforced bulk Cu-Fe immiscible alloy with nanotwinned Cu produced by selective laser melting, J. Alloys Compd. 838 (2020) 1–6, https://doi.org/10.1016/j. iallcom.2020.155592.
- [60] K.H. Zum Gahr, W. Bundschuh, B. Zimmerlin, Effect of grain size on friction and sliding wear of oxide ceramics, Wear 162–164 (1993) 269–279, https://doi.org/ 10.1016/0043-1648(93)90509-K.